



Preoperative path planning algorithm for lung puncture biopsy based on path constraint and multidimensional space distance optimization

Ling He^{a,*}, Yuxuan Meng^a, Jianquan Zhong^b, Ling Tang^b, Cheekong Chui^c, Jing Zhang^{a,*}

^a College of Biomedical Engineering, Sichuan University, Chengdu 610065, China

^b Department of Radiology, Zigong First People's Hospital, Zigong 643000, China

^c Department of Mechanical Engineering, National University of Singapore, Singapore 119077, Singapore



ARTICLE INFO

Keywords:

Surgical path planning
Lung biopsy
Constrained optimization
Multiobjective optimization
Pareto optimality

ABSTRACT

The quality of the clinician-planned puncture path significantly affects the success rate of percutaneous lung biopsy procedures. Therefore, a preoperative path planning algorithm for lung puncture biopsy is proposed to assist clinicians in planning the needle path of lung biopsy. First, lung tissues and organs are segmented based on CT images. Then, a multiple puncture target point approach is proposed to screen the target locations of suspected tumors. And the puncture needle path is determined after selecting the entry points on the skin. According to lung biopsy clinical requirements, three hard constraints are proposed to remove paths that do not meet clinical requirements. Additionally, six soft constraints and the Pareto optimization based on multidimensional space distance are proposed to obtain the optimal puncture paths. The experimental data were collected from 33 patients with suspected pulmonary nodules in the Zigong First People's Hospital. In the experiments, physicians labeled 98.46 % of the paths planned by the algorithm as clinically feasible, indicating that the proposed algorithm can be applied to nodule cases of different sizes and that it follows the clinical constraints of lung puncture. The average distance between the optimal algorithmic path and the surgical path was (5.77 ± 3.85) mm, which indicates that the proposed algorithm could simulate the surgical path according to the clinical guidelines of the physicians. The experimental results demonstrated that the proposed algorithm could provide an objective and effective path planning method for lung puncture biopsy of different nodule sizes.

1. Introduction and related work

Lung cancer is one of the most common form of cancers, with extremely high morbidity and mortality rates [1–4]. Nodular tumors appear in the lungs of patients with lung cancer, which lead to symptoms such as cough, shortness of breath, and chest pain [5]. Moreover, with the deterioration of the disease, the cancer cells will gradually transfer and spread to other tissues, causing various pathological changes to patients' tissues and organs [6].

Tumor diagnosis methods include medical history analysis, laboratory tests, physical examination, imaging examination, and pathological examination. Pathological examination is the gold standard for malignant tumor diagnosis [7]. Pathological examination of the lung involves obtaining the suspected tumor tissue by CT-guided lung biopsy, carrying out cytological examination on the obtained tissue, and finally obtaining the pathological results [6,8].

CT-guided lung biopsy is a challenging operation. Before performing

a lung puncture biopsy procedure, a CT scan of the patient's chest region is first performed. The physician uses the patient's CT images to determine the location of the suspected nodule and combines additional information obtained from the CT images to determine the patient's surgical position and the puncture entry point. During the execution of the procedure, the surgeon needs to perform a CT scan after needle advancement to observe the angle and depth of the needle advancement. Furthermore, according to the actual position of the puncture needle and the tumor, the needle advancement adjustment and CT scans are performed. This is repeated several times until the needle is advanced to the lesion site and the tissue sample is taken [9]. Depending on patient compliance, nodule accessibility, and the clinician's experience, the operation duration varies from 15 min to over one hour [10], and multiple needle insertions are performed in one operation [11,12]. The degree of injury and success rate of a patient's lung puncture surgery is limited by the skill and experience of the physician in pathway planning. Incorrect route planning may lead to penetration of normal tissues and

* Corresponding authors.

E-mail addresses: ling.he@scu.edu.cn (L. He), jing.zhang@scu.edu.cn (J. Zhang).

organs by the puncture needle. This further causes complications, including pneumothorax, pulmonary hemorrhage, hemopneumothorax, tumor metastasis, and implantation [13–15]. Moreover, faulty path planning can result in multiple needle entry adjustments, which increases the risk and possibility of complications. Repeated CT scans during the puncture also subject the patients to high-dose radiation in a short time [16,17]. Therefore, based on the aforementioned status of lung puncture biopsy surgery, optimizing the quality of lung puncture surgical path planning is necessary to assist clinicians in finding the optimal puncture path during lung puncture surgery more efficiently.

In order to improve the quality of surgical path planning, researchers have proposed an automatic surgical path planning technique with some preliminary results [18–23]. The automatic surgical path planning technique is based on preoperatively acquired CT images of the patients, and the optimal path is obtained by image processing and constrained optimization algorithms. The optimal puncture path and the patient's organs are displayed in three dimensions to assist clinicians in performing lung puncture surgery. Automated surgical path planning technology can reduce the influence of subjective factors on path planning, reduce the probability of complications and improve the success rate and efficiency of the surgery. Moreover, the automated surgical path planning technology reduces the number of punctures and the number of (CT) scans caused by path planning errors, reduces the total amount of radioactive radiation received during the operation, and reduces the invasiveness of the procedure. Therefore, this work aims to find an automated surgical path planning algorithm to assist clinicians in performing lung puncture procedures.

In the current research on automatic surgical path planning, constraint optimization methods are often used to automatically plan puncture paths in percutaneous surgery [24–26]. The steps are as follows. (1) The straight needle path is defined by the given target point (usually the centroid) and the entry points on the skin. (2) The constraints of the needle insertion point are divided into hard and soft constraints. Hard constraints are used to remove entry points on the skin where the trajectory formed by these insertion points and the target point violates the clinical guidelines [27]. Soft constraints that quantify the requirements that should be met as much as possible during the procedure are used to assess the quality of the remaining needle trajectories. Examples of these constraints include the distance to critical structures, path length, and the needle penetration angle [28]. (3) The optimal puncture path is obtained among the remaining paths using a multi-objective optimization algorithm based on multiple sub-objective functions of the remaining paths derived from the soft constraints. The existing research on constraint-based optimization for automatic path planning for percutaneous puncture focuses on the second and third steps [29].

Path constraints comprise hard and soft constraints [30,31]. Seitel et al. [32] proposed three hard constraints (occlusion, tangency, needle length) and two other hard constraints regarding the ablation area (safety margin around target, RFA-umbrella) in the automatic path planning of a liver ablation operation to determine the possible insertion areas on the skin. Three soft constraints (the distance to critical structures, trajectory length, and insertion angle) are used to evaluate the quality of the insertion area. Schumann et al. [33,34] considered four soft constraint parameters, insertion depth, distance from critical structure, vertical angle, and in-plane angle, to plan the path of the liver tumor ablation. Gao et al. [35] considered the shape and visible size of the tumor in craniofacial surgical path planning. Ren et al. [36] performed path planning for repeated multiple ablations of large tumors, and took into consideration the optimization of ablation coverage, the number of ablations, and the avoidance of critical structures. Li et al. [37] obtained the feasible puncture region through five hard constraints (anterior chest, path length, liver length ratio, critical structures, angle) and two ablation constraints (safety margin around the target, ablation needles). Then, four soft constraints (path length, distance to critical structures, puncturing angle, and ablation range efficiency) were

calculated to assist physicians in planning the ablation path of liver tumors. Baegert et al. [38] assisted the path planning of abdominal ablation surgery by considering two soft constraints: the actual needle depth and the actual distance from the needle path to the critical structure. He also used a geometric precipitator (based on the Nelder mead optimization algorithm) to optimize an elliptical model of the ablation volume. Chen [39] calculated a risk objective function for pulmonary puncture route planning based on the length of the puncture route and the radius of the tracheal vessels. Bao et al. [40,41] proposed three hard constraints, which are avoidance constraint, length constraint, puncture angle constraint, and soft constraints in terms of length, distance, and angle to quantify the clinical guidelines in pulmonary puncture procedures. Most of the current research on hard and soft constraints on surgical paths has focused on head and abdominal surgeries, with fewer constraints applicable to path planning for pulmonary puncture surgeries.

The weighted sum and Pareto methods are commonly used optimization algorithms in studies to obtain the best puncture path [29,32,42–44]. Baegert et al. [38] constructed an evaluation function to measure the soft constraints and combined the soft constraints with the weighted sum method. The retrospective clinical data of 7 cases verified the algorithm's feasibility in the abdominal percutaneous surgery path planning. Helck et al. [43] weighted the risk parameters considered for the puncture procedure, ranked the available trajectories, and then allowed the physician to select a clinical biopsy pathway manually. Zelmann et al. [44] calculated risk scores for intracranial electrode implantation planning trajectories by a weighted sum method, where weights were defined based on a questionnaire completed by three neurosurgeons. A retrospective trial of 20 patients showed that 95 % of the obtained algorithmic trajectories would be considered for clinical trials. The path planning method based on weighted summation are dependent on different weights given by clinicians [45], so this method is subjective, as it relies on the clinical experience of physicians, and increases the clinician's workload during the lung puncture procedure.

Recently, a few works have explored the path planning algorithm based on Pareto optimization [28,32,33,37,46,47]. Seitel et al. [32] planned the insertion trajectory by using the concept of Pareto optimality. The retrospective application of automatic trajectory planning to the CT data of 10 patients with complications after abdominal percutaneous surgery shows that the system may benefit radiologists. Schumann et al. [33] generated a cylindrical projection for each soft constraint parameter and normalized and weighted it to obtain initial optimal trajectories. Such trajectories were used to run local optimizations and return a solution approximating the Pareto front to obtain the optimal path. Li et al. [37] proposed a semiautomatic pretreatment planning method based on thermal ablation of liver tumors. The presented method takes DICOM images labeled with the masks of the organs and tissues as input and requires clinicians to predetermine the puncture times and puncture targets. The Pareto optimization is carried out through 4 optimization objectives to assist doctors in puncture path planning. Sun et al. [48] proposed a multilevel constraint strategy based on clinical puncture guidelines and combined the enclosed directional box hierarchical tree (OBBTTree) algorithm and the Pareto optimization algorithm to obtain the optimal puncture path. Bao et al. [28,40,41] proposed an intelligent lung biopsy path planning method based on multiobjective optimization. Six groups of chest CT data used six soft constraints and Pareto optimization concepts to find the optimal puncture path. In summary, most path planning studies based on Pareto optimization still require manual interaction in selecting the final path rather than fully automated path planning [29,37]. Moreover, there is no priority difference in each constraint objective function in Pareto optimization, which cannot simulate the clinically required puncture paths with short lengths and small angles in lung puncture procedures. Therefore, the Pareto optimization in the current study is not yet adapted to the clinical requirements of percutaneous lung puncture.

Based on the above, the research objectives of this work are: (1) Most

current studies are on path planning algorithms for abdominal and head surgeries. At the same time, there are fewer studies on path planning for lung puncture biopsy. This work quantifies the clinical requirements of lung puncture biopsy procedures into hard and soft constraints to make the surgical path planning algorithm suitable for lung puncture biopsy. (2) Currently, the weighting method has the limitation of requiring artificially set weights. The Pareto algorithm automatically calculates the optimal point without setting weights, but cannot simulate that physicians prefer paths with short lengths and small angles during puncture. Moreover, the current path optimization study still requires the physician to select the optimal path twice after using the Pareto method, which still increases the physician's workload in path planning. (3) The current studies on automatic path planning for lung puncture surgery have used the center of mass or center of the suspected tumor as the puncture target. However, the center or centroid of mass is not necessarily used as the puncture target point for large lung tumors in clinical practice. This work aims to explore a puncture target position extraction algorithm that applies lung puncture surgery. Therefore, a preoperative path planning algorithm for lung puncture biopsy based on path constraints and multidimensional space distance optimization is proposed. The planning path algorithm is made closer to the clinical gold standard to help physicians perform lung puncture biopsy procedures. First, lung tissues and organs are segmented based on patient CT data. Then, the puncture entrance positions on the skin and the puncture target positions on the tumor are selected to obtain the initial puncture path set. The paths that violate the puncture requirements are deleted from the initial path set by calculating three hard constraints. The six soft constraints of the constrained paths are calculated, and Pareto multiobjective optimization based on multidimensional distance is carried out by combining the soft constraint values to obtain the optimal puncture path.

Our method has the following contributions: (1) A preoperative path planning algorithm for lung puncture biopsy is proposed. Five hard constraints and six soft constraints are used to plan the lung puncture path, which integrates the current research study results and the clinician's clinical experience. Together with the improved multiobjective optimization, the optimal puncture path can be automatically planned to assist clinicians in path planning. (2) The proposed target position selection method is classified according to the size of suspected pulmonary nodules. The multiple puncture target position extraction method is proposed for type II suspected tumors. For type I suspected tumors, the needle path target point is set as the centroid. This method avoids the problem of limited puncture path selections due to a single target point and makes the path selection more flexible. (3) Lung puncture path planning is based on path constraints. Instead of selecting only the puncture entry points on the skin in existing literature, the paths consisting of the entry points and the target points are constrained and optimized, which provides an accurate puncture path selection range. (4) A Pareto optimization algorithm based on multidimensional space distance is proposed to optimize the puncture path. The weighted summation and Pareto optimization characteristics are combined, ensuring optimal multiobjective coordination that meets the clinical needs in lung biopsy.

Section 2 describes the proposed preoperative path planning algorithm for lung puncture biopsy. It includes organ tissue segmentation, path determination method, hard constraint, soft constraint, and multidimensional space distance optimization method. In **Section 3**, we compare the clinical experimental data to verify the feasibility of the path obtained by the proposed algorithm. Finally, in **Section 4**, the conclusions of the algorithm are shown.

2. Methods

Based on the lung puncture clinical standard, a preoperative path planning algorithm for lung puncture biopsy based on path constraint and multidimensional space distance optimization is proposed. The

algorithm is divided into five main steps, which are described as follows. First, the skin, lung parenchyma, and critical structures are segmented on the CT images. Subsequently, the puncture entry positions and the target positions are extracted to generate the initial needle paths. Then, three hard constraints for the needle path are extracted to eliminate inapplicable insertion paths in the initial needle paths set. Then, six soft constraints for the needle path are calculated to score the constrained path. Finally, together with six soft constraints, a Pareto optimization algorithm based on multidimensional space distance is carried out to obtain the optimal path. The overall puncture path planning process is shown in **Fig. 1**.

2.1. Preprocessing

Before lung puncture planning, the critical tissues and organs of the chest are segmented to provide the anatomical structure of each tissue and organ for the subsequent steps. The skin, lung parenchyma, bone, pulmonary vessel, trachea and bronchus, heart, and interlobar fissures are segmented using different segmentation algorithms.

First, the chest area is segmented by Otsu threshold processing and morphological operation [49]. The skin area is obtained by extracting the edge of the chest area, which is the initial feasible region for lung puncture path planning. Then, within the chest area, the 3D region growing algorithm is adopted to achieve lung parenchyma, bone, heart, trachea, and bronchus segmentation [50,51]. The blood vessels are segmented by the 3D multiscale Frangi-based lung vessel enhancement algorithm [52]. Finally, the pulmonary fissures are detected based on the FissureNet framework [53]. The lung nodules are manually labeled on CT images by clinicians.

2.2. Initial path determination

Each entry position in the skin and each target position in the suspected tumor together define a puncture path. In this process, the selection of the needle entry positions set E and the selection of the needle target positions set T are proposed to determine the initial paths P_{et} .

2.2.1. Entry position selection: Set E

The entry position selection enhances the method of taking the puncture needle entry position from the skin and screens the entry position from the skin surface area to ensure the puncture accuracy and reduce the calculation load. The skin area is the initial entry position, which is denoted as set E_0 . The entry position selection includes three parts: lung area extraction, heart area removal, and nipple and armpit area removal, which are described as follows.

Lung area extraction is performed to standardize the scope of the collected CT to the lung area. Before lung biopsy, the CT scanning area is manually determined by clinicians. The collected CT data may include the neck and abdomen. According to the segmentation results of lung parenchyma in **Section 2.1**, the areas beyond the lung area [**Fig. 2(a)**] are removed from the initial entry positions set E_0 .

The heart area cannot be punctured during lung puncture surgery. To ensure that the heart is not punctured, the projected area of the heart on the skin should be removed in the selection of the entry positions [**Fig. 2(b)**]. Based on the heart segmentation results obtained in **Section 2.1**, the heart is projected onto the skin surface along the sagittal direction. The heart projection area is removed from the initial entry positions set E_0 .

Clinically, nerves and blood vessels innervating the upper limbs are distributed in the armpits. Therefore, a lung biopsy cannot be performed on the armpit area. In addition, lung puncture cannot be performed on the nipple area of the patient's skin. MSER feature extraction and postprocessing are used to obtain the armpit area. Gamma correction and Harris corner detection are used to extract nipple points. Then, the armpit area and nipple area are eliminated from the initial entry positions set E_0 , as shown in **Fig. 2(c)**.

Entry positions set E is selected from set E_0 through three entry po-

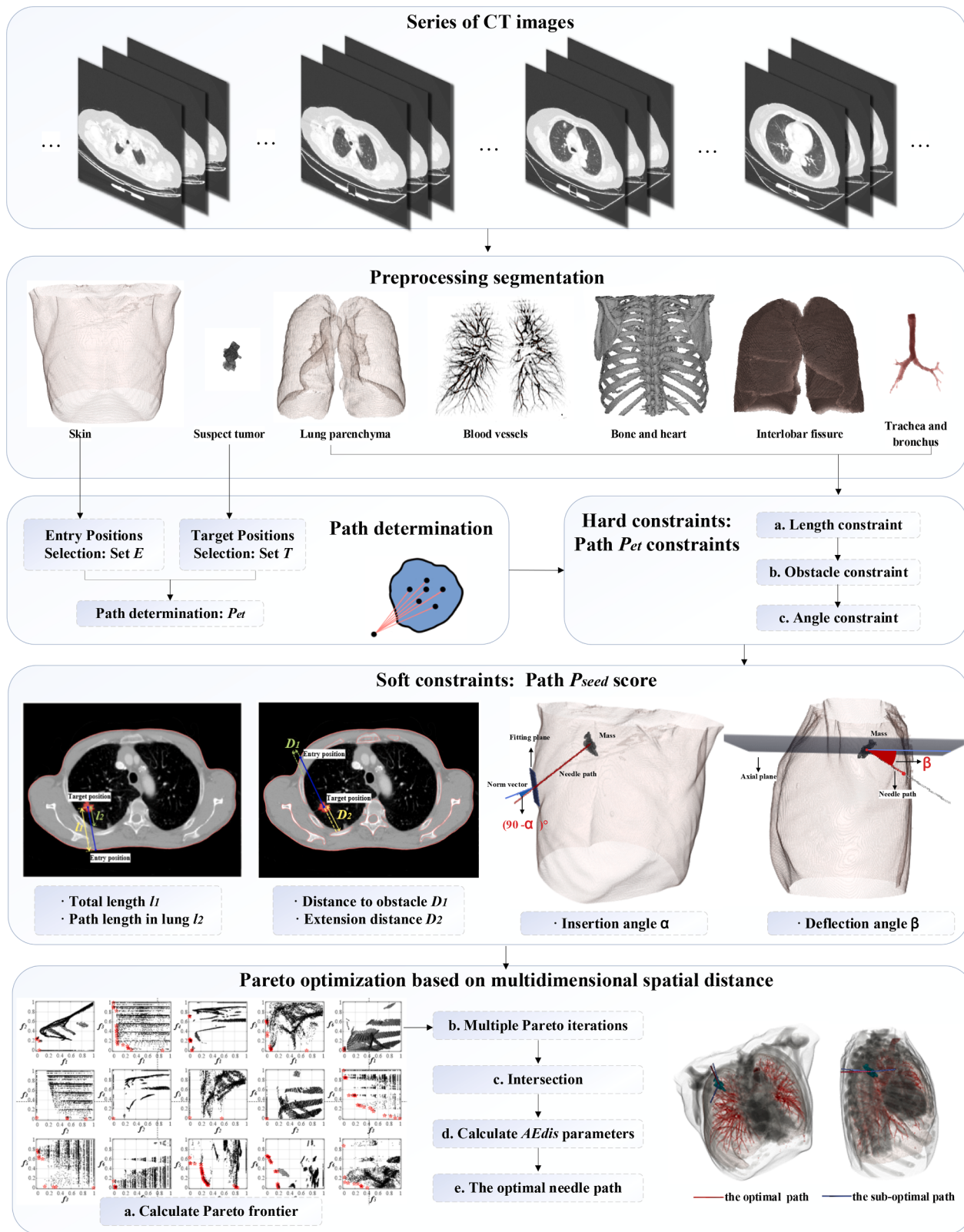


Fig. 1. Proposed puncture path planning algorithm flowchart.

sition selection steps, which standardizes the acquired CT range and removes the entry positions that cannot be punctured clinically.

2.2.2. Target position selection: Set T

A 0.5–1 cm long cylindrical sample with an intact lung nodule tissue

structure will be taken by a biopsy needle for pathological examination [54]. Therefore, during percutaneous lung biopsy, clinicians should ensure that the needle path in the suspected tumor area is within 0.5–1 cm.

Most current studies [55] take the centroid of suspected tumors as

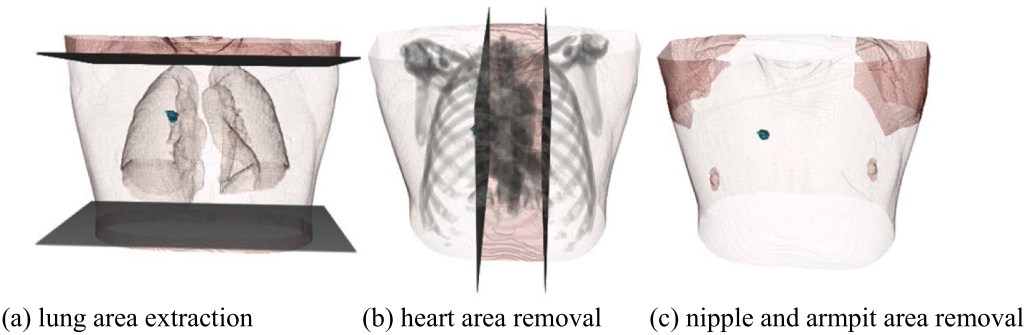


Fig. 2. Entry position selection result.

the puncture target position. However, in the clinical operation, the puncture target positions should be within 0.5–1 cm of the boundary of the suspected tumor area without aiming at the centroid for the puncture. Aiming at the centroid for puncture will narrow the path selection range, especially for large tumors [31]. Therefore, taking the centroid of the suspected tumor as the puncture target restricts the puncture path selection.

The target position selection method proposed in this paper is designed for different sizes of suspected tumors. Clinically, pulmonary nodules can be classified according to size [56]. Lung tumors with a diameter larger than 3 cm are called lung masses. If a lung tumor is three centimeters or less in diameter, it is commonly called a pulmonary nodule. The length of the puncture path in the suspected tumor needs to be 0.5–1 cm, so taking the centroid as the target point of the pulmonary nodule can meet the clinical requirements. Compared with pulmonary nodules, lung masses have a more comprehensive range of clinical puncture targets because of their larger size [57], and there is no need to aim at the centroid. The multiple target positions method is proposed for lung masses. The target position extraction method is described as follows.

(1) Classification of suspected tumor

According to the segmentation results of the suspected tumor in Section 2.1, the convex hull of 3D suspected tumor data points is found to obtain the suspected tumor boundary. Then, ellipsoid fitting is applied to the convex hull. The average diameter of the best-fit ellipsoid is calculated as the classification standard of the suspected tumor. The suspected tumor classification flowchart is shown in Fig. 3.

In this paper, suspected tumors with an average diameter of less than 3 cm are classified as type I suspected tumors. In comparison, those with an average diameter of more than 3 cm are considered type II suspected tumors. The details of these two following target position extraction methods are as follows.

(2) Target position extraction of type II suspected tumors

The target positions for type II suspected tumors are defined as a subregion in the suspected tumor via the following steps.

First, downsampling the suspected tumor area reduces repeating paths and computational redundancy. A needle path can be determined

by a pair of entry/target points. The search space is all combinations of the possible trajectories. Connecting one entry point to several target points may generate very close and even the same trajectories, as shown in Fig. 4(a), leading to calculation redundancy. It can be avoided by downsampling the dense target positions. Therefore, downsampling was performed using a 3 mm to 6 mm voxel grid, depending on the size of the suspected tumor, as shown in Fig. 4(b).

Then, the suspected tumor area is morphologically corroded. To ensure that 5 mm–10 mm long tissue samples can be taken by biopsy, the points within 5 mm–10 mm of the edge of the suspected tumor are removed. Morphological erosion (5 mm–10 mm) was applied to the segmentation result of the suspected tumor. [Fig. 5(b)].

Finally, the target positions are obtained by intersection of the downsampled points and the morphologically corroded tumor area, as shown in Fig. 5(c).

(3) Target position extraction of type I suspected tumors

For type I suspected tumors, the target position of the needle path is defined at the centroid of the suspected tumor. According to the segmentation results of the suspected tumor in Section 2.1, the centroid was calculated from all suspected tumor points. The result of extracting the target position of the type I tumor is shown in Fig. 6.

2.3. Hard constraints of the puncture needle path: Path P_{et} constraints

Based on the lung puncture surgery clinical standards, three hard constraints are proposed to restrict the puncture path set P_{et} . The violation of hard constraints will lead to a needle puncture failure and cause significant complications during an intervention.

In this work, the hard constraints of the puncture needle path are proposed as follows: (1) Length constraint: the length of the needle trajectory should be less than that of the biopsy needle. (2) Obstacle constraint: the needle paths are not allowed to pass through critical structures such as bones, large vessels, and nearby organs. (3) Angle constraint: the angle between the puncture needle and the skin surface should not be less than 20° .

The needle trajectories that violate hard constraints are eliminated from the puncture needle path set P_{et} . The puncture needle path set P_{et} consists of the paths determined by the points in the potential entry position set E and the points in the potential outlet position set T . The

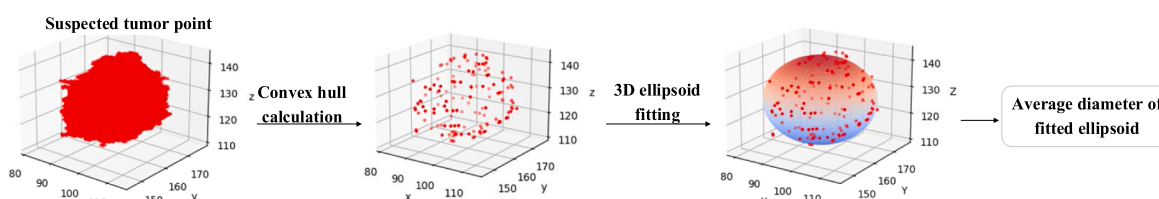


Fig. 3. Classification process of suspected tumors.



(a) Connecting one entry position to potential target positions

(b) Downsampling is used to reduce target positions

Fig. 4. Target position selection.

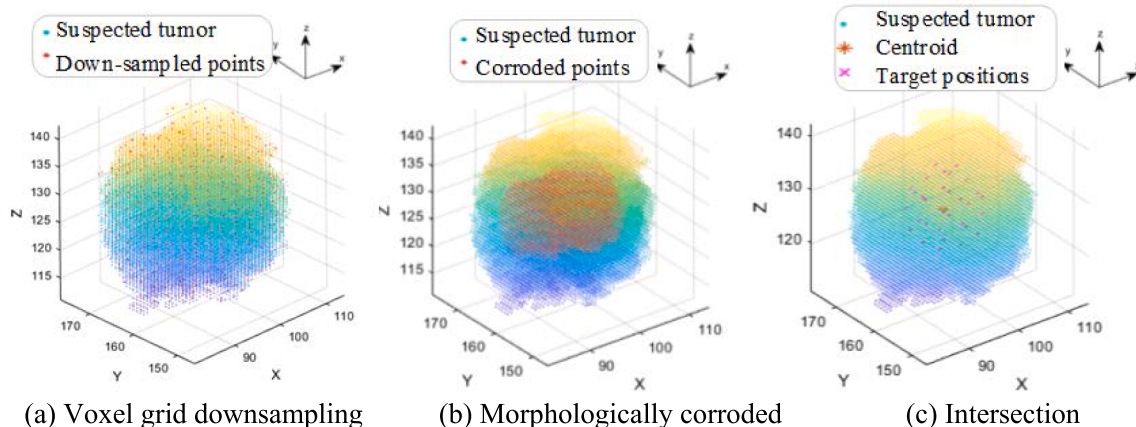


Fig. 5. Target position extraction of type II suspected tumor.

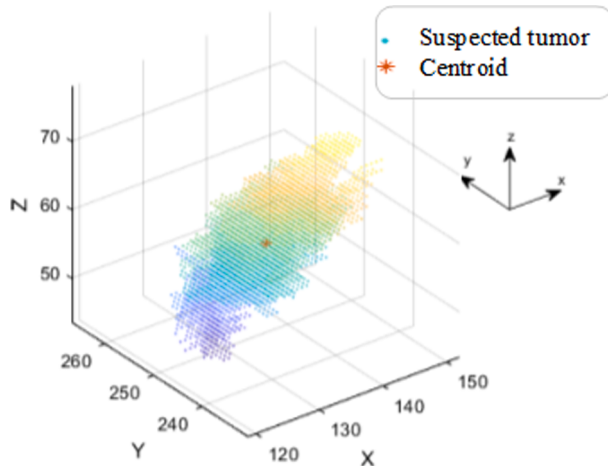


Fig. 6. Target position extraction of type I suspected tumor.

three hard constraints are described in detail in the following paragraphs.

2.3.1. Length constraint

To ensure that the lung nodule tissue samples are taken, the length of the needle trajectory l should be less than that of the puncture needle [58,59]. The mathematical expression of the needle trajectory l is as follows:

$$l = \left(|(x_E - x_T(i))M|^2 + |(y_E - y_T(i))N|^2 + |(z_E - z_T(i))K|^2 \right)^{\frac{1}{2}} \quad (1)$$

where (x_E, y_E, z_E) is the coordinate of the puncture entry point in the CT

image, which is the point in set E obtained from the skin region after the entry position selection in section 2.2.1, and (x_T, y_T, z_T) is coordinate of the puncture target point in the CT image, which is the point in the set T obtained from the suspected tumor region after the target position selection in section 2.2.2. These points are the coordinates of the CT pixel points calculated in the coordinate system of the patient's CT image. M and N are CT voxel spacing, K is CT slice spacing, and M, N, K are used to restore the original CT image to the actual 3D image size.

All puncture paths larger than the length of the puncture needle are eliminated from the feasible puncture path set P_{et} , and the puncture path set P_{length} with length constraint is obtained.

2.3.2. Obstacle constraint

The needle trajectory should avoid critical structures [60], including the heart, bone, vessel, trachea and bronchus, and interlobar fissures. The candidate puncture needle trajectories are obtained first by linear interpolation between each pair of entry/target points in the set P_{length} . Then, the candidate trajectories through the critical structures are removed according to the position of the critical structures, and the puncture path set $P_{obstacle}$ after the obstacle constraint is obtained.

2.3.3. Angle constraint

To prevent the puncture needle from slipping, the angle between the puncture needle and the skin surface θ should not be less than 20° [37]. Local surface fitting is performed in the neighborhood of the puncture entry positions, and the angle between the fitting plane and the puncture needle trajectory is calculated.

For each puncture entry point e_i , the least square local plane is fitted by its k neighboring points. The k -dimensional (K_D) tree [61] is used to find k points nearest to the puncture points e_i . This set is denoted by $Nbhd(e_i)$ and is called the k -neighborhood of e_i . Then, the least square method is used to fit the local plane T_p of $Nbhd(e_i)$. The local plane T_p fitting derived from the least square method is expressed as:

$$Tp(\mathbf{n}, d) = \underset{(\mathbf{n}, d)}{\operatorname{argmin}} \sum_{i=1}^K (\mathbf{n} \bullet \mathbf{e}_i - d)^2 \quad (2)$$

where \mathbf{n} is the normal vector of local plane Tp and d is the distance from the axis origin to the local plane $Tp(\mathbf{e}_i)$. Then, the normal vector solution of plane Tp is the eigenvalue decomposition of the local neighborhood covariance matrix M . The local neighborhood covariance matrix M of centroid $\bar{\mathbf{e}}_i$ is as follows:

$$M = \frac{1}{K} \sum_{j=1}^K (\mathbf{e}_{ij} - \bar{\mathbf{e}}_i) \bullet (\mathbf{e}_{ij} - \bar{\mathbf{e}}_i)^T \quad (3)$$

As M is a symmetric 3×3 positive semidefinite matrix, its three eigenvalues are all nonnegative. If $\lambda_i^1 \geq \lambda_i^2 \geq \lambda_i^3$ denote the eigenvalues of M , the unit eigenvector $\hat{\mathbf{v}}_i^3$ or $-\hat{\mathbf{v}}_i^3$ corresponding to λ_i^3 represents the normal vector \mathbf{n} of \mathbf{e}_i . As the centroid $\bar{\mathbf{e}}_i$ is inside the curved surface, the opposite direction is the normal direction.

With the normal vector \mathbf{n} obtained by the local plane fitting, the angle θ between the normal vector \mathbf{n}_i of \mathbf{e}_i and the puncture candidate trajectory vector \mathbf{l}_i is calculated, as described by Eq.(4).

$$\theta = \operatorname{abs} \left(90 - \arccos \frac{\mathbf{n}_i \bullet \mathbf{l}_i}{\|\mathbf{n}_i\| \|\mathbf{l}_i\|} \right) / 180\pi \quad (4)$$

The needle path whose angle with the skin surface is less than 20° is removed from the puncture path set $P_{obstacle}$, and the set P_{seed} of seed puncture paths is obtained.

2.4. Soft constraints of the puncture needle path: Path P_{seed} score

The feasible solutions of needle path planning are further explored by soft constraints. Soft constraints represent the requirements that should be satisfied as much as possible in treatment planning. In this work, the soft constraints for the puncture needle path are proposed as follows: (1) Soft constraints related to the needle path length: the total length of the needle path and the length of the needle path in the lung should be as short as possible. (2) Soft constraints related to needle path distance: the distance between critical structures and the needle path and the distance between the path extension line and the critical structures should be large enough. (3) Soft constraints related to the needle insertion angle: the needle should be inserted into the skin as vertically as possible.

The previously determined seed path set P_{seed} is rated by the soft constraints. The rating value of the soft constraint is normalized such that it is in the range of [0,1]. A rating value of 0 refers to an invalid trajectory, while a rating value of 1 refers to a trajectory that is considered relatively safe. The proposed soft constraints of the puncture needle path are described below.

2.4.1. Soft constraints related to needle path length

During the percutaneous needle biopsy of the lung, the biopsy needle is inserted through the skin into the patient's lung to the site of a suspected tumor. The length of the puncture path should be short enough to prevent tissue damage caused by needle deviation.

The total length l_1 represents the total length of the needle path. The intrapulmonary length l_2 denotes the needle path length in the lung. A schematic illustration of l_1 and l_2 is shown in Fig. 7, which is drawn on a 2D plane for convenient representation. The mathematical formulas of l_1 and l_2 are as follows:

$$l_1(i) = \left(|(x_E - x_T(i))X|^2 + |(y_E - y_T(i))Y|^2 + |(z_E - z_T(i))Z|^2 \right)^{\frac{1}{2}} \quad (5)$$

$$l_2(i) = \left(|(x_T - x_P(i))X|^2 + |(y_T - y_P(i))Y|^2 + |(z_T - z_P(i))Z|^2 \right)^{\frac{1}{2}} \quad (6)$$

where (x_E, y_E, z_E) is the puncture entry point and (x_T, y_T, z_T) is the puncture target point. (x_P, y_P, z_P) is the intersection of the i -th needle path and the pleural surface. X is the pixel spacing in the x-dimension, Y

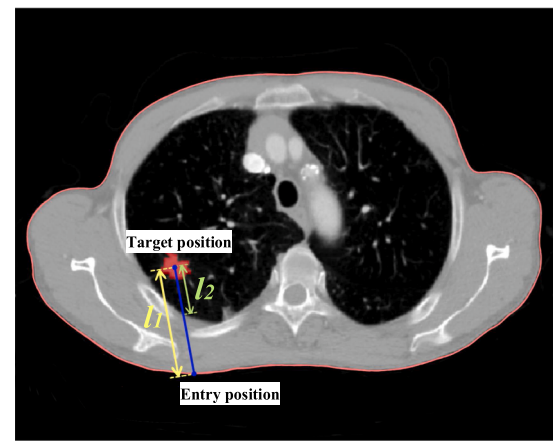


Fig. 7. Illustration of l_1 , l_2 .

is the pixel spacing in the y-dimension, and Z is the slice spacing.

The rating functions f_1 and f_2 are defined by normalizing l_1 and l_2 , respectively. The min–max normalization method is used to normalize l_1 and l_2 , as shown in the following formula:

$$f_1(i) = \frac{l_1(i) - l_{1min}}{l_{1max} - l_{1min}} \quad (7)$$

$$f_2(i) = \frac{l_2(i) - l_{2min}}{l_{2max} - l_{2min}} \quad (8)$$

where l_{1min} and l_{1max} are the minimal and maximal values of l_1 , respectively. l_{2min} and l_{2max} are the minimal and maximal values of l_2 , respectively.

2.4.2. Soft constraints related to needle path distance

The needle path should be far enough from critical structures to prevent complications by puncture deviation. The distance to obstacle D_1 is defined as the shortest distance between the puncture needle trajectory and any point of the critical structures. A schematic illustration of D_1 is shown in Fig. 8, which is drawn on a 2D plane for convenient representation. In this work, the steps for calculating D_1 are as follows: (1) the critical structure points are stored in a K-dimensional tree (K_D -tree), in which the points closest to the puncture trajectory are looked up; (2) for each point of the puncture trajectory, the minimum distance to the critical structures is calculated; and (3) the distance to critical structures D_1 is obtained by comparing the minimum distance from all the path points to the critical structures. The rating of the distance to critical structures constraint f_3 is calculated from D_1 as follows:

$$f_3(i) = 1 - \frac{D_1(i) - D_{1min}}{D_{1max} - D_{1min}} \quad (9)$$

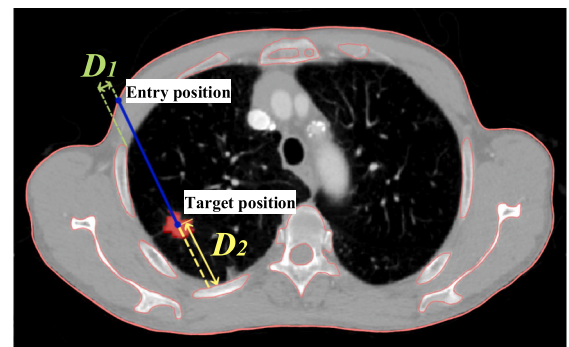


Fig. 8. Illustration of D_1 , D_2 .

where $D_1(i)$ is the distance from the i -th path to the critical structures, D_{1min} and D_{1max} are the minimal and maximal distances to the critical structures, respectively.

The needle tip usually exceeds the predefined target point in the clinic to ensure that enough physiological tissues are obtained. Therefore, the distance between the path extension line and critical structures should be large enough; otherwise, it may cause deep penetration touching critical structures during a lung needle biopsy. The extension distance D_2 denotes the distance between the extension line of the needle path and critical structures. The critical structures here refer to bones, pulmonary vessels, trachea and bronchus, heart, interlobar fissures, and skin, which have been extracted in section 2.1. Note that the definition of D_2 must be present because the skin must be present on the extension of the needle path. A schematic illustration of D_2 is shown in Fig. 8, which is drawn on a 2D plane for convenient representation. The path points from the target points along the extension line are searched until they hit the critical structures points. The distance from this point to the target points is calculated and denoted by D_2 . The rating of the extension line constraint is calculated from D_2 as follows:

$$f_4(i) = 1 - \frac{D_2(i) - D_{2min}}{D_{2max} - D_{2min}} \quad (10)$$

where $D_2(i)$ is the distance between the i -th path extension line and critical structures. D_{2min} and D_{2max} are the minimal and maximal trajectory extension distances, respectively.

2.4.3. Soft constraints related to needle insertion angle

During percutaneous lung biopsy, physicians should insert the needle into the skin as vertically as possible. The insertion angle α and the deflection angle β are calculated in our process, the details of which are described in the following paragraph.

The insertion angle α is defined as the angle between the needle path and the skin surface. The method of calculating the insertion angle α is described in the previous section (Section 2.3.3. Angle constraint). The rating of the insertion angle f_5 is calculated by normalizing α , and its equation is as follows:

$$f_5(i) = \frac{\log_{10}(\alpha(i)/20^\circ)}{\log_{10}(90^\circ/20^\circ)} \quad 20^\circ < \alpha(i) \leq 90^\circ \quad (11)$$

where $\alpha(i)$ is the insertion angle of the i -th needle path.

Clinically, the physician-recommended puncture path is oriented parallel to the CT slicer plane [37], as this is easier for the physician to reproduce the puncture in practice and is safer for the patient. Moreover, the small angle of the puncture needle to the CT plane during the operation reduces the number of CT image layers to be generated and viewed [32], optimizing the workflow during the intervention [34]. The

deflection angle β denotes the angle between the needle path and the axial plane where the target point of the needle path is located, as shown in Fig. 9. The deflection angle β should be small enough. The rating of the deflection angle $f_6(i)$ is calculated by normalizing $\beta(i)$, and its equation is as follows:

$$f_6(i) = \exp(-\beta(i)/20^\circ) \quad (12)$$

where $\beta(i)$ is the deflection angle of the i -th needle path.

2.5. Pareto optimization based on multidimensional spatial distance

After defining the hard constraints and soft constraints, the optimal needle path is planned under the constraints. The needle path optimization involves the decision-making and numerical optimization of multiple-objective functions. The optimization objective functions include path length f_1 , intrapulmonary length f_2 , distance to critical structures f_3 , extension distance f_4 , insertion angle f_5 , and deflection angle f_6 . The values of optimization objective functions should be as small as possible. The variable to optimize is the coordinate value (x, y, z) , which are the coordinates of the entry/target points in the seed path set P_{seed} . The mathematical model of the multiobjective optimization problem is as follows:

$$\begin{aligned} \min F(X) = & [f_1(X), f_2(X), f_3(X), f_4(X), f_5(X), f_6(X)]^T \\ X \in & P_{hard} \\ X = & (x, y, z) \end{aligned} \quad (13)$$

where P_{seed} is the seed puncture path set. Thus, the global optimal solution set P_{opt} is searched in the seed puncture path set P_{seed} .

Pareto optimization based on multidimensional space distance is proposed and utilized in this process to select the optimal path set P_{opt} from all seed puncture paths. This work introduces the concept of Pareto optimization to the path planning of lung puncture surgery. Pareto optimality is a widely used multiobjective optimization method that is ideal for resource allocation [62]. Pareto optimality means that in the parameter space, for solution A , all objective function values for which no other solution can be found in the parameter space are better than the objective function values corresponding to solution A [63]. The Pareto-optimal solution set is also called the Pareto front. The proposed optimization method combines the characteristics of the Pareto optimal method and the weighted sum method, and avoids the deviation caused by subjective factors in the weighted sum method [45]. It also avoids the disadvantages of the Pareto optimal method, which makes it difficult to simulate clinicians' preference for puncture paths with shorter paths and smaller deflection angles [37]. The steps of the proposed optimization method are shown in the following paragraphs.

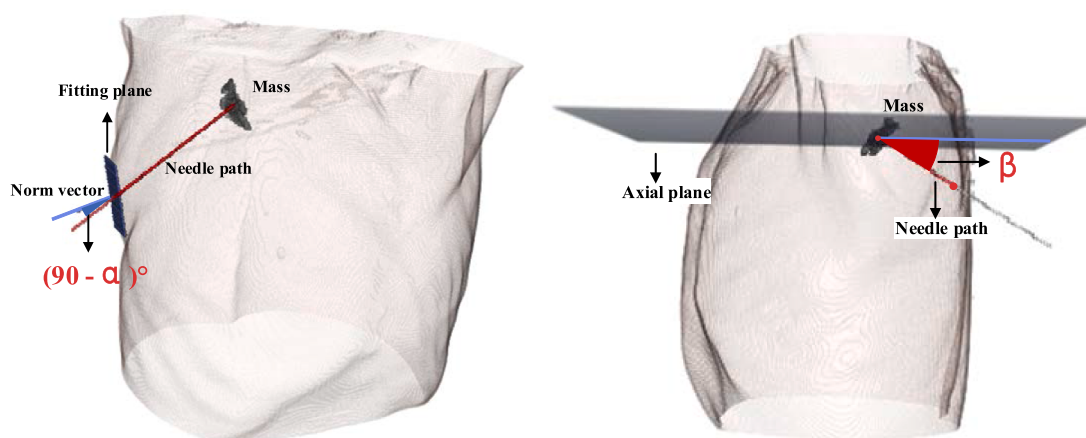


Fig. 9. Illustration of angle α , β .

- (1) A Pareto coordinate system is established with every two optimization sub-objectives. Therefore, 15 (C_6^2) coordinate systems are established according to 6 sub-objective functions, as shown in Fig. 10. The points in Fig. 10 represent the seed puncture paths calculated by hard constraint, and the horizontal and vertical coordinates of the points correspond to the two sub-objective function values of the seed puncture path respectively. According to the concept of Pareto optimization [64], the set of Pareto front points is calculated and marked with red stars in Fig. 10. The paths corresponding to the obtained front points are the optimal path solutions under two sub-objectives. Take the first figure in Fig. 10 as an example. The horizontal axis is the path length f_1 , and the vertical axis is the intrapulmonary length f_2 . A small value of the sub-objective function indicates low risk for the corresponding path. The points marked by red stars are the Pareto front points derived from the Pareto optimality. There are no other points in this coordinate system whose two sub-objective function values are all smaller than the two sub-objective function values of these points.
- (2) After extracting the Pareto frontier points, they are removed from the coordinate system. Note that each coordinate system only removes the front points obtained in this coordinate system. Then, the Pareto frontier points of the remaining point set are extracted again. Repeat this step for multiple Pareto iterations. The frontier point set obtained in the i -th iteration is denoted by frontier level L_i ($i = 1, 2, \dots, n$), and its schematic diagram is shown in Fig. 11.

The number c of each point that appears in the obtained Pareto frontier points is recorded. The iteration stops when the number of extracted front points exceeds half of the total number. Then, the point with $c = C_6^2$ is selected as the frontier point to be selected from the obtained frontier points. Fig. 12 shows the Pareto optimal candidate point set obtained after the iteration in two three-dimensional coordinate systems. The XYZ axes of the two coordinate systems represent six sub-objective functions.

- (3) The puncture risk of the path decreases with the decrease in its objective function value. Moreover, some sub-objective functions are contradictory because the decrease in one sub-objective

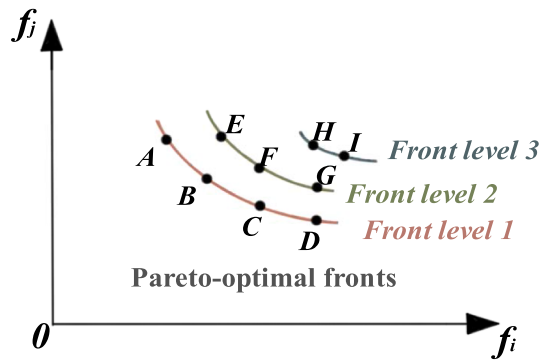


Fig. 11. Schematic diagram of each Pareto front level.

function value will increase the results of the other objective functions to varying degrees. In our method, to comprehensively consider the risks of length, angle, and distance and combine the clinical habits of clinicians, the *AEdis* (aligned Euclidean distance) is proposed. (Clinically, physicians prefer the needle path with a smaller puncture angle and shorter length.) *AEdis* comprehensively measures the distance between a vector and an ideal point in a six-dimensional space. Assume that the sub-objective function values of the ideal point are all 0. The *AEdis* between six-dimensional vectors $X(f_1, f_2, \dots, f_6)$ and ideal point $I(0, 0, \dots, 0)$ is calculated as follows:

$$AEdis(X(i)) = c_{X(i)} \bullet \sqrt{\sum_{k=1}^n r_k \bullet (f_k(i) - f_{k,min})^2} \quad (14)$$

where vectors $X(i)$ and their coordinates represent the six sub-objective function values of the i -th puncture path. $f_{k,min}$ is the minimum of $f_k(i)$, and $c_{X(i)}$ is the number of points appearing in the Pareto frontier point set. r_k defines the weight value that clinicians set for the k -th sub-objective function according to clinical experience.

Based on the Pareto front point set obtained in (2), the *AEdis* of each puncture path is calculated by Eq. (14). The points whose values are less than the mean value of *AEdis* are extracted as the optimal path set P_{opt} . In the optimal path set P_{opt} , the path with the smallest *AEdis* value is the optimal path, and the rest are suboptimal paths. The optimal path is

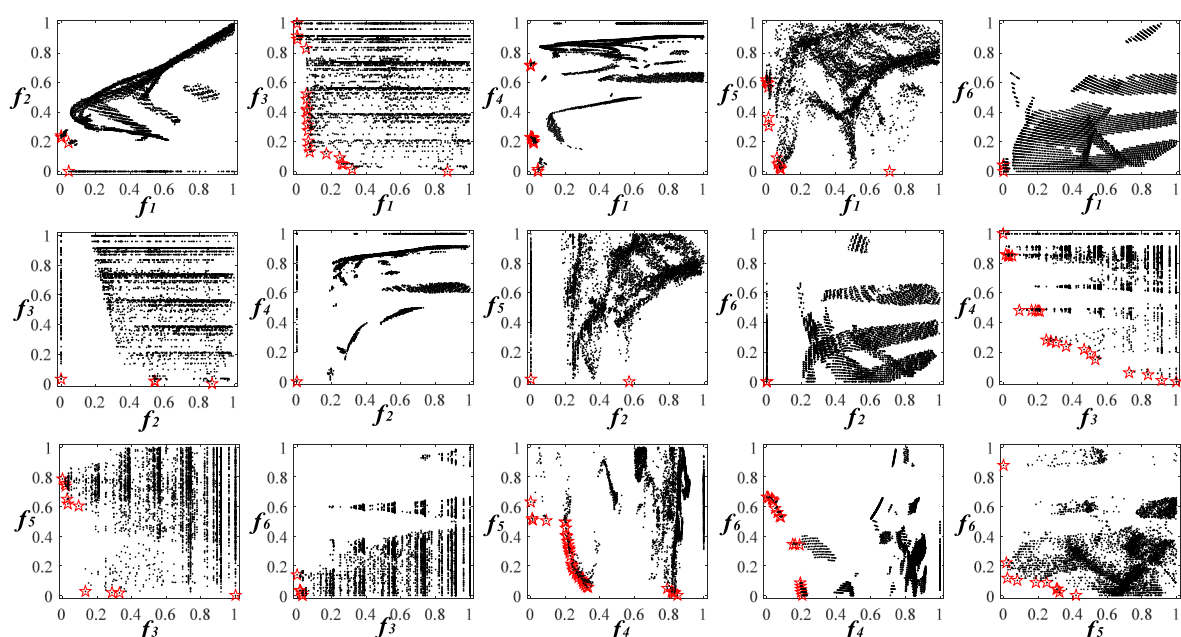


Fig. 10. Pareto coordinate system and Pareto front.

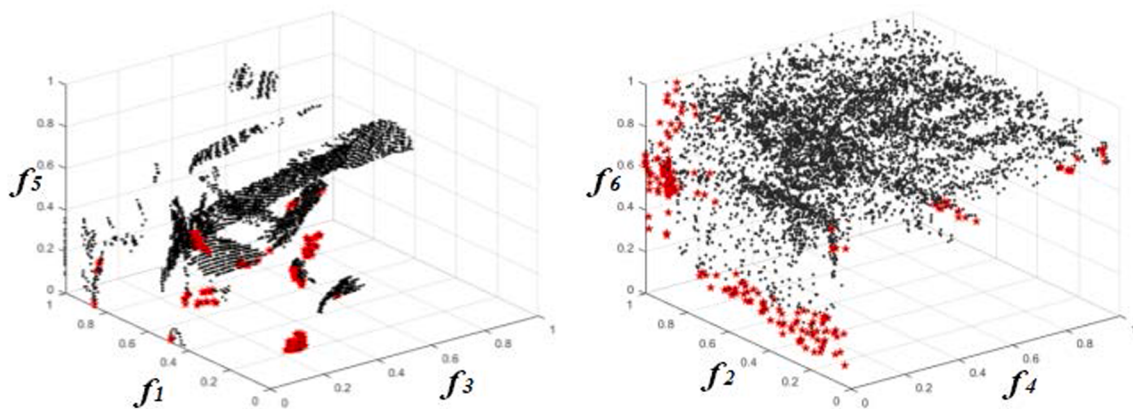


Fig. 12. Pareto optimal candidate points obtained after iteration.

displayed in red, and the other alternate paths are displayed in blue, as shown in Fig. 13.

3. Results

3.1. Experimental data

To evaluate the performance of the preoperative path planning algorithm for lung puncture biopsy based on path constraint and multi-dimensional space distance optimization, CT images of 33 patients with suspected lung tumors were collected from the Zigong First People's Hospital. Zigong First People's Hospital is a tertiary comprehensive hospital with rich clinical experience in lung puncture surgery and can provide sufficient clinical data and experienced guidance. This study was reviewed and approved by the Medical Ethics Committee of Zigong First People's Hospital (No. Ethics (Research) –2020–98). All participants signed their informed consent prior to their inclusion in this research.

The collected chest CT data of 36 patients are called the Lung Puncture CT dataset (LPCT). The Lung Puncture CT dataset is divided into two parts. One part is the CT data of 25 patients scanned before lung biopsy surgery, called the Nonoperated LPCT dataset (NLPCT). The other part is the CT data of 8 patients scanned before and after successful lung biopsy, called the Operated LPCT dataset (OLPCT). Among these CT images, the pixel size varies from 0.576 mm to 0.957 mm, the slice

thickness is 1 mm and 1.5 mm, the in-plane resolution is 512×512 , and the slice number varies from 161 to 245.

3.2. The experimental results and analysis of the retrospective study

A retrospective study was used to verify the performance of the proposed algorithm. In this section, based on the OLPCT dataset, the proposed algorithm is used to plan the lung puncture path. The planning results were displayed in three dimensions and qualitatively evaluated by two clinicians. Four indicators were proposed to quantitatively evaluate the path obtained by the algorithm, which are described in the following paragraphs. The path obtained by the proposed algorithm is simply referred to as the algorithm path.

A retrospective study was used to verify the performance of the proposed algorithm. In this section, based on the OLPCT dataset, the proposed algorithm is used to plan the lung puncture path. The path obtained by the proposed algorithm is simply referred to as the algorithm path. The planning results were displayed in three dimensions and qualitatively evaluated by two clinicians. The optimal algorithm path was compared quantitatively with the surgical path. Four metrics are proposed to evaluate the similarity of the two needle paths in three-dimensional space, which are described in the following paragraphs.

(1) ANND:

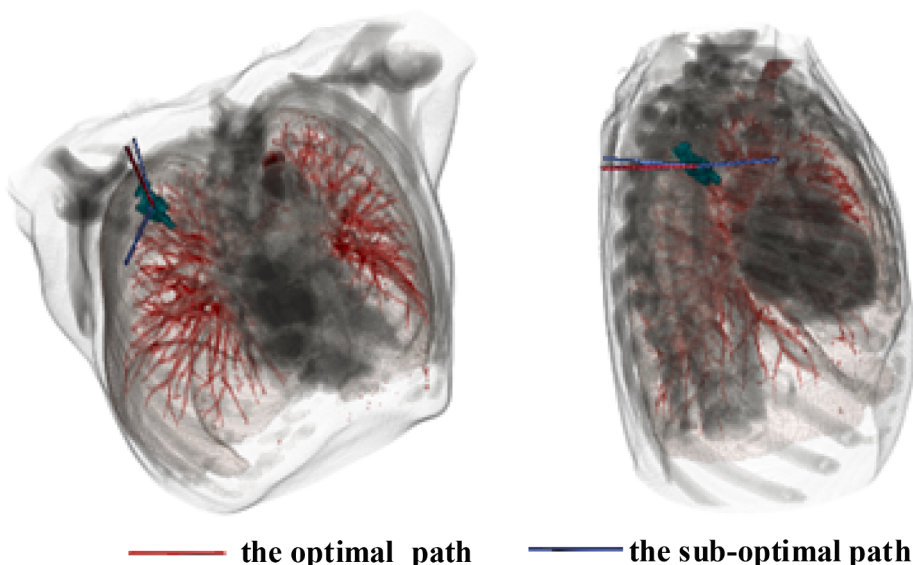
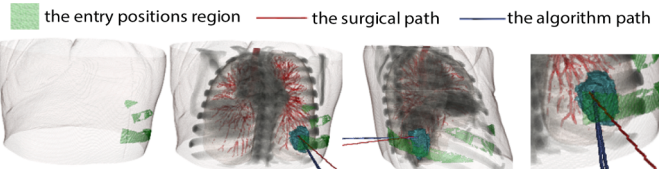
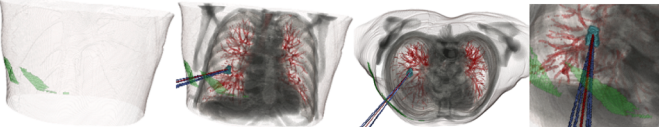
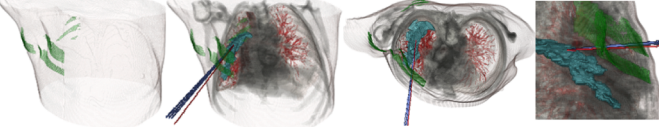
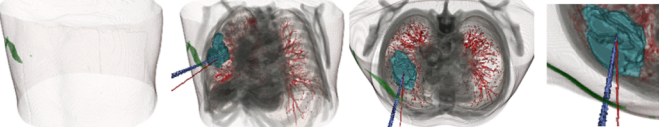
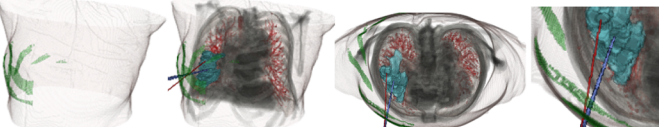


Fig. 13. 3D display of needle paths obtained by the proposed algorithm.

The ANND (average nearest neighbor distance) is proposed to evaluate the average distance between the optimal algorithm path and surgical path in 3D space. The points on the optimal algorithm path obtained by the proposed algorithm are defined as $O = \{o_1, \dots, o_m\}$. The points on the surgical path are defined as $S = \{s_1, \dots, s_n\}$. The formula of ANND is as follows:

$$\text{ANND}(O, S) = \frac{1}{m} \bullet \sum_{i=1}^m \min_{s \in S} \|o_i - s\| \quad (15)$$

Table 1
Evaluation results of the proposed algorithm on OLPCT dataset.

ID	Result diagram of surgical path and algorithm path	ANND (mm)	ED (mm)	Ang (°)	CosSim
1		3.20	14.49	6.77	0.79
2		2.30	2.28	2.41	0.81
3		1.11	1.76	2.41	0.98
4		3.74	11.00	7.15	0.93
5		7.28	14.90	17.55	0.72
6		12.06	30.51	34.56	0.87
7		6.62	9.03	11.41	0.97
8		9.84	13.66	7.98	0.90

Here, $\min_{b \in B} \|o_i - s\|$ is the distance between each point o_i in point set O and the point s_j in the set S closest to point o_i , and m is the number of points in point set O.

(2) ED and Ang

The ED (entry point distance) is presented to calculate the Euclidean distance between the entry point of the optimal algorithm path and the surgical path. The Ang is proposed to calculate the angle between the

optimal algorithm path vector and surgical path vector.

(3) Cosine similarity *CosSim*:

The cosine similarity *CosSim* is proposed to evaluate the similarity between the soft constraint scores of the surgical path and the optimal algorithm path. A large *CosSim* value indicates similar vectors. The soft constraint score vector of the optimal algorithm path is defined as $f_o = [f_{o,1}, \dots, f_{o,6}]$. The soft constraint score vector of the surgical path is defined as $f_s = [f_{s,1}, \dots, f_{s,6}]$. The *CosSim* between f_o and f_s is defined as follows:

$$\text{CosSim}(O, S) = \frac{\sum_i f_{o,i} f_{s,i}}{\sqrt{\sum_i f_{o,i}^2} \sqrt{\sum_i f_{s,i}^2}} \quad (16)$$

where $f_{o,i}$ and $f_{s,i}$ denote the i -th soft constraint score of the optimal algorithm path and surgical path, respectively.

The evaluation results of the proposed algorithm based on the OLPCT dataset are shown in Table 1. Among them, the quantitative comparison results of the optimal algorithmic path and surgical path based on four index values are shown in Table 1. Moreover, the lung puncture path planning results obtained by the proposed algorithm based on the OLPCT dataset are displayed in three dimensions, including the algorithm paths, lung tissue structures, and the surgical path, as shown in the second column of Table I. Moreover, the views in different directions and the zoomed-in view are provided to facilitate better understanding of the path deviation. The algorithm needle paths, the surgical path, and the entry positions region are marked in blue, red, and green, respectively, by pseudocolor processing. Two clinicians with experience in lung biopsy surgery evaluated the clinical feasibility of the algorithm needle paths. N_{in} and N_{total} represent infeasible algorithm paths evaluated by clinicians and the number of all algorithm paths, respectively, and the N_{in} and N_{total} of each case are shown in Table 1.

In the second column of Table 1, $N_{in} = 0$ indicates that the number of clinically infeasible paths in lung puncture biopsy procedures obtained by the proposed algorithm as concluded by the physicians on the OLPCT dataset is 0. Therefore, the algorithm paths obtained in the retrospective experiment of these eight cases are clinically feasible. The physicians indicated that they could follow the algorithm paths for puncture procedures. Moreover, it can be qualitatively seen from the experimental results in different views provided in Table 1 that the resulting algorithmic paths and clinical paths are similar in 3-dimensional space and that the location of the puncture entrance is consistent with the location of the entrance to the surgical path. It can be seen from Table 1 that the algorithm paths avoid critical tissue structures, including the trachea, bone, heart, etc. Furthermore, the puncture positions corresponding to the algorithm paths are consistent with the puncture position corresponding to the surgical path. These indicate that the proposed algorithm can accurately avoid each critical tissue according to the clinical constraints of the lung puncture procedure and avoid the occurrence of complications due to planning errors that result in punctures to critical structures.

The results of the quantitative evaluation of the optimal path obtained by the proposed algorithm in the retrospective experiment with 8 cases are also shown in Table 1. Table 1 shows that the *ANND* between the optimal algorithm path and the surgical path is (5.77 ± 3.85) mm. The entry distance *ED* between the optimal algorithm path and the surgical path is (12.20 ± 9.01) mm. The *Ang* between the optimal algorithm path and the surgical path was $(11.28 \pm 10.60)^\circ$. The *CosSim* value is 0.87 ± 0.09 . The overall distances between the optimal algorithm paths and the surgical paths are all below 1.3 cm, and the distances between the entry points are also below 3.1 cm, which indicates that the 3-dimensional spatial distance between the optimal algorithm paths and these optimal algorithm paths are concentrated in areas near

the surgical paths. Moreover, the average angle of the 3-D vectors corresponding to the optimal algorithm paths and the clinical paths is 11.28° , and the average cosine similarity of the corresponding 3-D vectors is 0.87, which indicates that the optimal algorithm path is highly similar to the clinical path. It further shows that the proposed algorithm can accurately plan the surgical path according to the clinical requirements without violating the clinical guidelines for lung puncture surgery. It also simulates the clinician's preference in lung puncture surgery path planning. The standard deviation of the four indices of eight cases ranges from 0.09 to 10.6, which shows the robustness of the proposed algorithm.

The evaluation results of 8 cases in four indices indicate that the proposed algorithm can be applied to CT data of patients with different types of suspected tumors. For type I suspected tumors in cases No. 2 and No. 4, the *ANND* distance between the optimal algorithm path and the surgical path is less than 4 mm, and the *Ang* is less than 8° , which indicates that the optimal algorithm path is close to the surgical path.

Since the target position of the type I suspected tumor is the centroid, which is close to the target point of the surgical path, the path distance of the type I suspected tumor mainly depends on the distance of the entry position, and a small *ED* value leads to a small *ANND* value. The *ED* and *ANND* values of cases No. 2, 4 are less than 1.2 cm, which further indicates that the proposed algorithm can plan clinically feasible paths for the type I suspected tumor. Cases Nos. 1, 3, 5, 6, 7, and 8 are CT data of patients with type II suspected tumors. In these cases, the small *ANND* parameter for measuring the average distance between two paths indicates that the optimal algorithm path is concentrated near the surgical path. In cases Nos. 1, 5, and 8, the *ANND* between the optimal algorithm path and the clinical path is less than 10 mm, while the *ED* is greater than 10 mm. The patients in these three cases had type II suspected tumors. In the target position selection method (illustrated in Section 2.2.2), the target point selection range of type II suspected tumors is larger than that of type I suspected tumors. The distance of the target point between the optimal algorithm path and the surgical path offsets the entry point (*ED*) distance, resulting in the optimal algorithm path being still close to the surgical path.

In case No. 6, the *ANND* and *ED* were greater than 10 mm, and the *Ang* was larger than 30° , while clinicians indicated that the optimal algorithm path obtained in case No. 6 was clinically feasible. Since the surgical path was almost parallel to the transverse plane, the optimal algorithm path was mainly away from the clinical path in the direction perpendicular to the CT slicers. This shows that although the indices of the optimal algorithm path were better than those of the surgical path, it was difficult for physicians to grasp the angle and direction of the optimal algorithm path in clinical operation.

3.3. Experimental results and analysis of the prospective study

A prospective study was performed on the NLPCT database containing preoperative chest CT data of 25 patients with suspected tumors. The needle path obtained by the proposed algorithm and lung tissues and organs was displayed in three dimensions, as shown in Fig. 14. The optimal algorithm path, the suboptimal paths, and the entry positions region are marked in red, blue, and green, respectively, by pseudocolor processing. Two clinicians with lung puncture experience calibrated the clinical feasibility of the algorithm needle paths. The number N_{in} of algorithm paths determined as infeasible by clinicians and the total number N_{total} of algorithm paths are shown in Fig. 14.

Fig. 14 shows that the number N_{total} of needle paths planned for each case ranges from 2 to 7. Except for cases Nos. 9 and 16, clinicians identified the number of clinically infeasible algorithm paths in the remaining 23 cases was 0 ($N_{in} = 0$). This shows that the proposed algorithm has good performance in lung biopsy path planning on the NLPCT dataset. Moreover, combined with the experimental results in Section 2.3, the algorithm obtained 130 algorithmic paths in 33 cases, 98.46 % of which were marked as clinically feasible by the physicians.

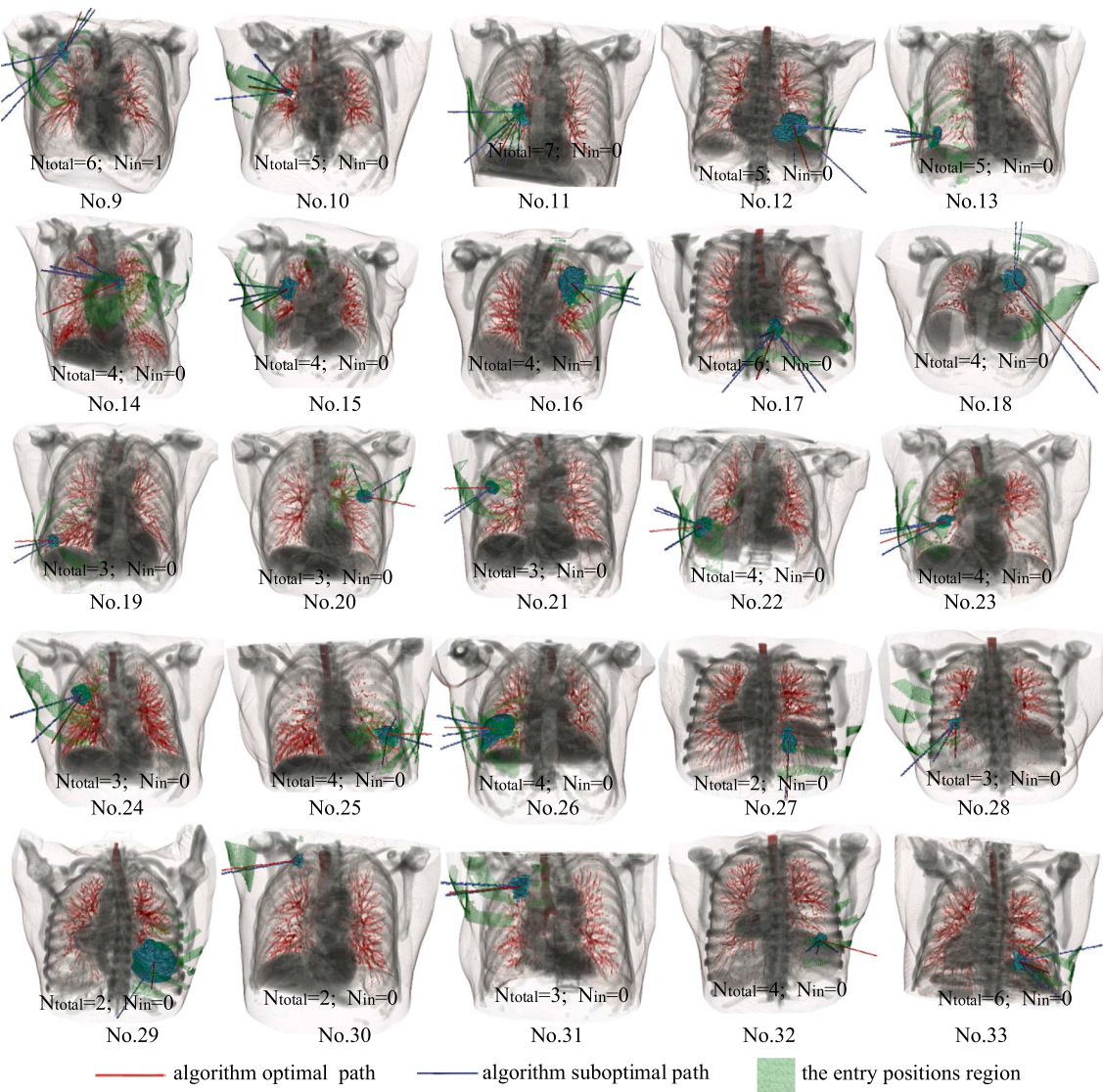


Fig. 14. Planning results obtained by the proposed algorithm based on the NLPCT dataset.

This demonstrates the robustness of the proposed lung puncture path planning algorithm. In all cases of the NLPCT dataset, the puncture path planned by the proposed algorithm avoided critical structures such as bones, heart, and bronchi, which indicates that the hard constraint (illustrated in Section 2.3) and entry position selection (illustrated in Section 2.2.1) in the proposed algorithm are effective in obstacle avoidance. Furthermore, it can be seen from the figure that the path planned by the proposed algorithm is on the same side of the chest as the tumor making the path length small, and most of the paths are perpendicular to the skin and the paths are at a small angle to the CT plane. This indicates that the path optimization algorithm can simulate the clinician's preference for paths with small lengths and deflection angles during the lung puncture procedure.

In cases No. 9 and No. 16, clinicians calibrated that there was a clinically infeasible path in the suboptimal algorithm paths. Compared with other algorithm paths, the infeasible path was longer in total path length l_1 , and its deflection angle β with reference to the transverse section was larger, which made it difficult for clinicians to reproduce the angle and direction of the path during a lung biopsy.

3.4. Constraint strength of the hard constraint

The hard constraint is used to remove needle paths that violate the

medical regulations of percutaneous lung biopsy. For 33 sets of patients' CT data in the LPCT dataset, the constraint strength of the hard constraint is evaluated by four indices. The constraint strength R_s of entry position selection is the proportion of the entry points removed by the entry position selection method (illustrated in Section 2.2.1) to skin points, and its mathematical formula is as follows:

$$R_s = (\text{num}(E)/\text{num}(E_0)) \times 100\% \quad (17)$$

where $\text{num}(E)$ and $\text{num}(E_0)$ respect the number of entry points removed by entry position selection and the number of initial entry points on the skin, respectively.

The constraint strengths R_H of three hard constraints (length constraint illustrated in Section 2.3.1, obstacle constraint illustrated in Section 2.3.2, and angle constraint illustrated in Section 2.3.3) are the proportion of the needle paths removed by a certain hard constraint to the corresponding input paths, and the formula is as follows:

$$R_H = (\text{num}(P_{H,\text{con}})/\text{num}(P_{H,\text{input}})) \times 100\% \quad (18)$$

where $\text{num}(P_{H,\text{input}})$ and $\text{num}(P_{H,\text{con}})$ denote the number of paths restricted by a specific hard constraint and the number of input paths in the current hard constraint, respectively.

The constraint strengths of the four parts are listed in Table 2. Note

Table 2

Constraint strength of the hard constraint based on the LPCT dataset. (S = entry position selection; H1 = length constraint; H2 = obstacle constraint; H3 = angle constraint).

Case ID	$R_S(\%)$	$R_{H1}(\%)$	$R_{H2}(\%)$	$R_{H3}(\%)$
1	78.29	36.20	57.76	20.85
2	76.42	9.97	88.27	11.65
3	77.36	17.36	68.31	12.31
4	77.74	27.04	85.84	7.83
5	80.88	2.77	90.80	23.39
6	74.64	8.99	82.02	14.70
7	79.84	25.40	90.69	1.43
8	75.30	1.42	71.01	8.92
9	75.39	2.72	76.52	3.38
10	74.98	62.03	40.42	14.31
11	77.12	55.03	32.46	13.96
12	81.53	20.36	78.11	17.39
13	70.44	0.74	54.57	42.09
14	70.03	10.94	59.42	14.04
15	71.54	3.23	64.23	2.34
16	75.06	0.08	62.96	19.28
17	70.31	44.86	62.19	10.18
18	76.05	16.37	65.55	4.93
19	73.38	6.65	65.96	51.42
20	76.29	0.38	59.02	43.39
21	78.86	17.17	67.50	8.08
22	75.40	0.45	65.33	13.78
23	71.61	0.32	62.65	14.10
24	70.35	0.98	64.82	2.03
25	68.68	4.15	65.19	21.82
26	75.87	0.17	66.54	9.18
27	70.31	44.59	62.43	10.19
28	73.32	17.92	70.73	7.64
29	78.73	13.59	68.34	7.04
30	84.25	0.00	74.60	4.25
31	65.68	28.35	60.27	4.91
32	81.67	34.42	70.38	10.11
33	81.49	48.89	64.80	4.20
Mean	75.42	17.08	67.26	13.79

that, based on the order of the proposed algorithm execution, the input of the latter column is based on the constraint result of the previous column rather than the constraint results of each column for the initial set of punctured paths. In addition, the comparison result of the four-step constraint strength is also visually shown in Fig. 15. In the figure, the four constraint strength values calculated from the same case are superimposed on the ordinate and displayed in different colors. The abscissa indicates the case number and the ordinate indicates the superimposed values of the constraint strengths.

As can be visualized in Table 2 and Fig. 16, each constraint effectively removes paths that do not meet the corresponding clinical criterion as a basis of the optimal selection of subsequent paths. Among the four constraint strengths, the entry point location selection has the highest constraint strength, and the angle constraint has the lowest constraint strength. Table 2 shows that the number of entry points removed by entry position selection accounts for a large proportion of all skin points, with an average of 75.42 %. Entry position selection is used

to remove the skin points beyond the lung area and the skin parts that cannot be punctured, including the heart area, the armpit, and the nipple area. Since this step involves many critical skin areas, the constraint strength R_S of entry position selection is greater than that of other hard constraints.

The average constraint strength of obstacle constraint R_{H2} is 67.26 %, much higher than that of length constraints and angle constraints. It is caused by the ribs, sternum, and spinal bones in critical organs. The puncture needle path can only pass through the gaps of these bones. In addition, critical structures cannot be punctured in the lung parenchyma surrounded by bones, such as large blood vessels and bronchi. Therefore, the obstacle constraints can remove a large number of puncture needle paths.

Compared with the obstacle constraint, the constraint strength R_{H1} of the length constraint is smaller. Most skin points far away from the suspected tumor were deleted in entry position selection, resulting in an input path larger than the removed puncture needle.

The constraint strength R_{H3} of the angle constraint is the smallest of the four parts. Since the input paths with angle constraints have been restricted by multiple constraints, most paths that do not meet clinical constraints are removed before the input angle constraint.

The final feasible path solution is obtained step by step through three constraints in the initial path solution set. However, the order of the solution has an influence on the efficiency of the algorithm. The angle constraint with the highest complexity of the algorithm is implemented in the last step, which can minimize the number of computations in this step. Similarly, the length constraint with the lowest algorithm complexity is executed in the first step, which also reduces the number of computations for the obstacle constraint in the next step.

3.5. Comparison of target point selection methods

In the current surgical path planning studies, Seitel, Scorza, and Zhang et al. [29,31,32] set the target point of the needle path as the center or centroid of the suspected tumor. Li et al. [37] used the path target point manually marked by the physician as the target point for path planning in their work. The coverage of the lesion is used as a condition for path target point selection in path planning studies based on ablation procedures [19]. These methods of target point selection are not applicable to pathway planning for lung puncture biopsy due to the different clinical constraints of different procedures. Moreover, taking the centroid as the target point of path planning is not accurate for large-sized suspected tumors because clinicians only need to ensure that the 0.5 ~ 1 cm long tissues are taken from the suspected tumors in clinical operation [54]. In the proposed target position selection method (illustrated in Section 2.2.2), the suspected tumors are classified according to their size, the target position of the type I suspected tumor is set as the centroid, and the target positions of the type II suspected tumor are set as its internal 3D subregion.

To verify the effectiveness of the proposed algorithm, the target position selection method proposed in this paper is compared with the target point selection method proposed in existing research. The experiment was carried out on a large-OLPCT dataset, which included CT data of 6 patients with type II suspected tumors in the OLPCT dataset.

The comparison results of the optimal algorithm paths obtained by the two target point selection methods in terms of four indices are listed in Table 3. In addition, the comparison results of the optimal paths obtained by these two methods are also intuitively shown in Fig. 16.

Table 3 shows that the ANND of the optimal algorithmic path obtained by setting the centroid as the target point is (16.50 ± 5.32) mm, while the ANND of the optimal algorithm path obtained by the proposed target position selection method (illustrated in Section 2.2.2) is (6.69 ± 4.06) mm. It indicates that the optimal path obtained by the proposed algorithm is closer to the clinically used path in 3D space than the optimal path obtained by the centroid target point method. In terms of the ED and Ang indices, the index value of the optimal algorithm path

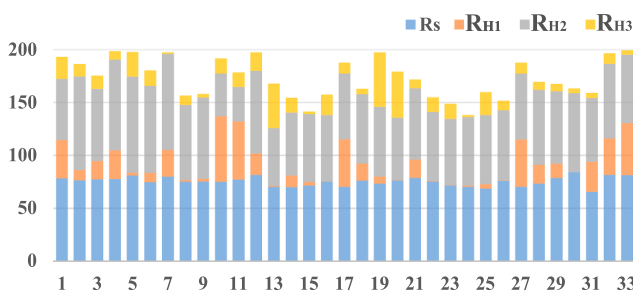


Fig. 15. Constraint strength of the hard constraint based on the LPCT dataset.

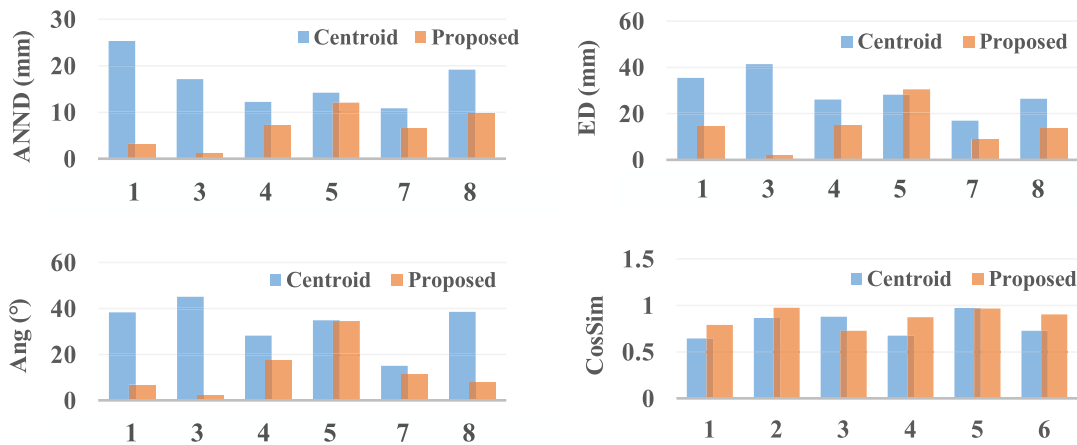


Fig. 16. Comparison results of two point selection methods on the large-OLPCT dataset.

Table 3
Comparison results of two point selection methods on the large-OLPCT dataset.

Case ID	Method	ANND (mm)	ED (mm)	Ang (°)	CosSim
1	Centroid [29,31,32]	25.35	35.46	38.29	0.64
	Proposed	3.20	14.49	6.77	0.79
3	Centroid [29,31,32]	17.15	41.41	45.11	0.87
	Proposed	1.11	1.76	2.41	0.98
5	Centroid [29,31,32]	12.21	26.14	28.24	0.88
	Proposed	7.28	14.90	17.55	0.72
6	Centroid [29,31,32]	14.21	28.14	34.88	0.67
	Proposed	12.06	30.51	34.56	0.87
7	Centroid [29,31,32]	10.86	16.96	15.08	0.97
	Proposed	6.62	9.03	11.41	0.97
8	Centroid [29,31,32]	19.19	26.40	38.55	0.73
	Proposed	9.84	13.66	7.98	0.90

obtained by the centroid target point method is greater than that obtained by the proposed method. It indicates that the optimal algorithmic path obtained by the centroid target point method deviates from the clinical path where there is a large distance between the path entry point and the entry point of the clinical path relative to the optimal algorithmic path obtained by the proposed method. Moreover, the cosine similarity *CosSim* of the optimal algorithm path obtained by the centroid target point method is lower than that of the proposed method. Combining the four index values, the paths obtained by the proposed method are closer to the clinical paths than those obtained by the centroid target point method. Clinicians do not aim at the centroid of the suspected tumor for the puncture in lung puncture surgery. They take the whole tumor area as the target point of the puncture and ensure that a sample of 0.5 cm-1 cm can be taken from the target area during the puncture. Clinicians are very flexible in selecting the target points of type II suspected tumors, and the selected areas of the target points for type II suspected tumors are more than those for type I suspected tumors. Therefore, the centroid target point method has poor performance in four indices.

3.6. Comparison of the multiobjective optimization method

The application of multiobjective optimization algorithms in percutaneous puncture path planning is still in the research stage. In the current path optimization for surgical path research, two and more subjective functions of candidate surgical paths are calculated, such as path length, puncture angle, and other objective functions. Then the optimal path corresponding to the optimal solution is obtained by a multiobjective optimization solution based on multiple objective functions. There are two common multiobjective optimization methods in

the application of surgical path planning: the weighted summation algorithm and the Pareto multiobjective optimization method. The multiobjective optimization method based on weighted sum is widely used in surgical path planning [32,35,38,40,43,44,45,66]. The weighted sum method gives weights to multiple soft constraints and then sums them up for optimization. The formula is shown below:

$$\min \sum_{i=1}^m w_i \cdot f_i \quad (19)$$

where w_i defines the weight of the i -th soft constraint, f_i denotes the value of the i -th soft constraint, and m represents the number of soft constraints. Zelmann et al. [44] used a weighted sum method to optimize the path to improve the risk score of the planned trajectory for intracranial electrode implantation, where the weights were defined based on a questionnaire completed by three neurosurgeons. The results showed that 95 % of the algorithmic trajectories obtained in 20 cases were clinically feasible. Helck et al. [43] used a weighted sum method to rank the available trajectories and then allowed the physician to select the clinical biopsy path manually. Zhang [65] used weighted processing of constraint maps for automatic planning of the hepatic ablation needle puncture path, and 78 % of the algorithmic paths were clinically valid in 10 cases of data. However, the weights in the weighted sum method are set by the doctor, which depends on the doctor's clinical experience and introduces errors caused by subjective factors into the path planning [45].

To avoid the interference of artificial factors of weighted summation, some researchers gradually proposed surgical path planning based on Pareto optimization [28,37,40,41,45,48,67]. Li et al. [37] calculated four optimization objectives for the thermal ablation of liver tumors performed Pareto optimization, and realized that Pareto optimization could effectively achieve surgical path planning. Sun et al. [48] proposed a multilevel constraint strategy based on clinical puncture guidelines combined with the Pareto optimization algorithm to obtain the puncture path. They verified the effectiveness of the algorithm through simulation experiments. Bao et al. [28,40,41] divided the six soft constraints into three groups, established a Pareto coordinate system with two soft constraints in each group, and solved the intersection of the best points in the three coordinate systems to obtain the optimal path of lung puncture. Furthermore, the application of Pareto and the weighted method in surgical path planning is compared. The experimental results demonstrate that the path obtained by the Pareto method has better index values than the path obtained by the weighted summation method under multiple objective conditions. The Pareto optimization method can objectively find the optimal points under multiple constraints. However, it is challenging to meet the surgical requirements that a path with a shorter length and smaller deflection angle is easier for

clinicians to perform.

The Pareto optimization method based on multidimensional space distance proposed in this paper combines the characteristics of the above two methods. Based on six soft constraints, the proposed algorithm calculates Pareto optimal points in fifteen Pareto coordinate systems and carries out multiple Pareto optimal iterations to obtain multiple Pareto optimal points. Then, according to the weight set, the *AEdis* distance of Pareto frontier points after the intersection is calculated to obtain the optimal needle path.

The multiobjective optimization method proposed in this paper is compared with two optimization methods commonly used in existing research regarding four indices on the OLPCT dataset. The comparison results are shown in Table 4 and Fig. 17. Note that among the paths obtained by the Pareto method, we choose the path with the smallest mean of *ANND* and *ED* for comparison.

The results of the weighted sum method on the OLPCT dataset in terms of the four indices are 13.34 ± 12.45 mm, 45.82 ± 49.71 mm, $40.87 \pm 49.58^\circ$, and 0.76 ± 0.24 . Compared with the proposed method, the weighted sum method has larger average values of *ANND*, *ED*, and *Ang* and smaller average values of cosine similarity *CosSim*. The standard deviation of the weighted sum method in four indices is greater than that of the proposed method in four indices, which indicates that the performance of the weighted sum method in four indices is unstable on the OLPCT dataset.

In cases No. 4 and No. 7, compared with the other two methods, the weighted sum method has larger values in *ANND*, *ED*, and *Ang* and smaller values in *CosSim*, which indicates that the paths obtained by the weighted sum method are closer to the surgical path. However, in the remaining cases, the weighted sum method has poor performance in four indices. The ideal weighted result is not equivalent to the cooperative optimization of the multiobjective vector function. Moreover, the weight factors of the weighted sum method depend on subjective experience, which causes planning deviation.

The results of the Pareto optimization method on the four indices are 6.77 ± 3.73 mm, 16.32 ± 10.88 mm, $15.01 \pm 11.92^\circ$, and 0.76 ± 0.29 . According to the average of four indices, it can be seen that the optimal path obtained by Pareto optimization is closer to the surgical path than that obtained by weighted sum. The standard deviation of the Pareto optimization algorithm in four indices is less than that of the weighted sum method, which shows that the Pareto optimization algorithm is more robust. The Pareto optimization method avoids the interference of

human factors of the weighted sum method and can comprehensively coordinate the parameters to achieve the optimum. However, compared with the proposed method, the Pareto optimization method has poor performance in four indices. Since the Pareto method is a multiobjective collaborative optimization, it is difficult to simulate that clinicians prefer to choose a path with a shorter length and smaller deflection angle in lung puncture path planning.

The average values of the proposed method on the four indices are 5.77 ± 3.85 mm, 12.20 ± 9.01 mm, $11.28 \pm 10.60^\circ$, and 0.87 ± 0.09 , respectively. Among the three methods listed in Table 4, the standard deviation of the four indices obtained by the proposed method is the smallest, the mean value of *ANND*, *ED*, and *Ang* is the smallest, and the mean value of *CosSim* is the largest. It shows that the paths obtained by the proposed method have the greatest similarity with the surgical path. The proposed method combines the characteristics of the weighted sum method and the Pareto optimization method. It can coordinate the multiobjective function while choosing the path that clinicians can operate more easily. The minimum standard deviation of the four indices also shows that the proposed algorithm is robust to various CT data and lung puncture cases.

4. Conclusion

A preoperative path planning algorithm for lung puncture biopsy based on path constraint and multidimensional space distance optimization was proposed. Based on the CT data of 33 patients with pulmonary nodules, a retrospective study and a prospective study on the algorithm were carried out. In the retrospective study, the results of the algorithm on the four indices of *ANND*, *ED*, *Ang*, and *CosSim* were 5.77 ± 3.85 mm, 12.20 ± 9.01 mm, $11.28 \pm 10.60^\circ$ and 0.87 ± 0.09 , respectively, and the algorithm paths were all marked as clinically feasible by clinicians. In the prospective study, only two algorithm paths were calibrated to be clinically infeasible. The results show that the algorithm paths were effectively calculated to be close to the actual surgical paths, hence proving the feasibility and robustness of the proposed algorithm in lung puncture path planning.

The proposed algorithm directly uses DICOM images of CT data as input, segments tissues and organs of the lung, and then combines path constraints with a multiobjective optimization algorithm to obtain the optimal surgical path. Target position selection (illustrated in Section 2.2.2) expands the range of path selection and makes path planning

Table 4
Comparison results of three multiobjective optimization methods on the OLPCT dataset.

Case ID	Method	N	ANND (mm)	ED (mm)	Ang (°)	CosSim
1	Weighted sums [32,35,38,40,43,44,45,46,47]	1	3.98	15.02	5.90	0.68
	Pareto optimality [28,37,40,41,45,48,67]	3	3.59	13.46	3.92	0.41
	Proposed	2	3.20	14.49	6.77	0.79
2	Weighted sums [32,35,38,40,43,44,45,46,47]	1	4.93	4.24	7.77	0.79
	Pareto optimality [28,37,40,41,45,48,67]	2	2.67	4.65	4.70	0.97
	Proposed	5	2.30	2.28	2.41	0.81
3	Weighted sums [32,35,38,40,43,44,45,46,47]	1	38.26	174.11	143.12	0.71
	Pareto optimality [28,37,40,41,45,48,67]	6	3.94	6.51	8.28	0.89
	Proposed	5	1.11	1.76	2.41	0.98
4	Weighted sums [32,35,38,40,43,44,45,46,47]	1	2.03	5.59	4.31	0.97
	Pareto optimality [28,37,40,41,45,48,67]	5	4.18	9.91	9.06	0.97
	Proposed	2	3.74	11.00	7.15	0.93
5	Weighted sums [32,35,38,40,43,44,45,46,47]	1	12.33	24.32	26.51	0.22
	Pareto optimality [28,37,40,41,45,48,67]	2	8.67	17.38	20.50	0.22
	Proposed	4	7.28	14.90	17.55	0.72
6	Weighted sums [32,35,38,40,43,44,45,46,47]	1	14.41	41.55	43.85	0.92
	Pareto optimality [28,37,40,41,45,48,67]	6	13.34	37.29	40.50	0.88
	Proposed	3	12.06	30.51	34.56	0.87
7	Weighted sums [32,35,38,40,43,44,45,46,47]	1	6.25	8.03	10.41	0.86
	Pareto optimality [28,37,40,41,45,48,67]	4	8.73	14.85	16.92	0.99
	Proposed	5	6.62	9.03	11.41	0.97
8	Weighted sums [32,35,38,40,43,44,45,46,47]	1	24.54	93.72	85.05	0.90
	Pareto optimality [28,37,40,41,45,48,67]	5	9.07	26.53	16.20	0.72
	Proposed	4	9.84	13.66	7.98	0.90

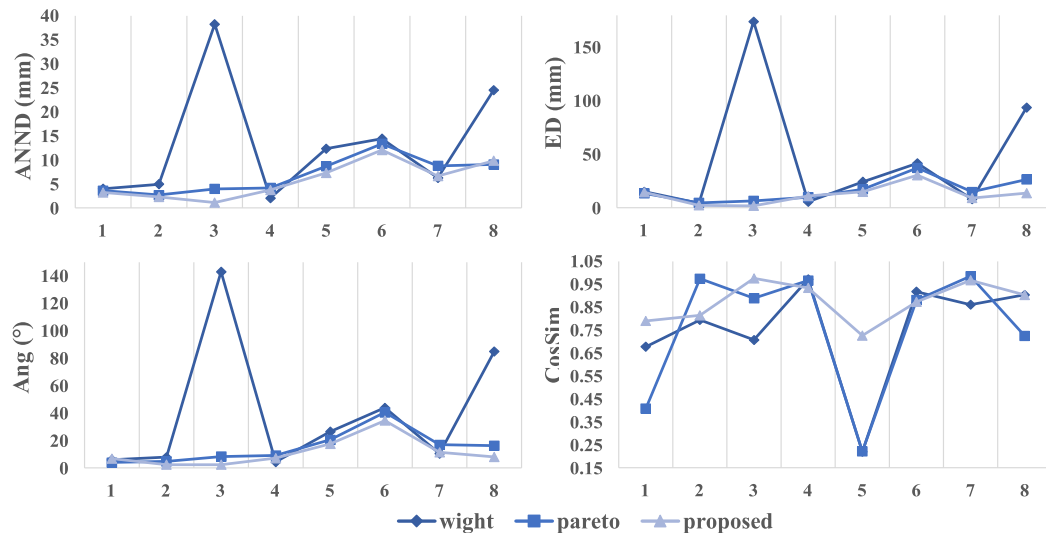


Fig. 17. Comparison results of three multiobjective optimization methods on the OLPCT dataset.

precise and accurate, which accords with clinical practice. Path constraint limits the puncture path to a reasonable puncture range according to several clinical standards. Pareto optimization based on multidimensional spatial distance can comprehensively consider the characteristics of the weighted sum method and the Pareto method based on six soft constraints. It can coordinate multiple parameters while considering the shared preferences of clinicians in an operation.

The proposed preoperative path planning method of lung puncture biopsy can effectively produce the puncture path and facilitate preoperative path planning in lung puncture surgery. It avoids the dependence of artificial path planning on the doctors' professional knowledge and clinical experience and reduces path deviation caused by human factors. The proposed method can improve the success rate of lung biopsy, reduce the incidence of complications and shorten the operation time.

The shortcomings and outlook of this work are summarized as follows. (1) The present work is based on preoperative path planning of the patient's scanned CT images before surgery. The work is not real-time because the preoperative path planning allows sufficient time for the surgeon to evaluate and even modify the algorithm to plan the path. In future works, the relationship between clinical needs and real-time will be better weighed, and the program will be modified to make it lighter to investigate intraoperative surgical path planning further. (2) Since the lung puncture needle used in clinical practice is a rigid puncture needle [7], the degree of the needle during puncture is small [68]. In this work, the impact of the needle on path planning is not considered, and only preoperative path planning is done to assist the physician in the puncture biopsy procedure. In future work, since there will be deformation of the needle and soft tissue organs during puncture, the investigation of deformation rules will involve soft tissue mechanical models and biological experiments. Therefore, we will further investigate the mechanical interaction mechanism between the puncture needle and soft tissues after supplementing the data with relevant biological tissue and needle samples. The study of the patient's respiratory motion acquisition and prediction will also be conducted to assist the physician in guiding the puncture motion in the temporal dimension.

Funding

This work was supported by the National Natural Science Foundation of China [Grant No 61571314]; the Zigong Key Science and Technology Plan Task [2020xy02]; and the Sichuan University-Yibin City Strategic Cooperation Special Fund Project [2020CDYB-27].

CRedit authorship contribution statement

Ling He: Conceptualization, Formal analysis, Resources. **Yuxuan Meng:** Methodology, Software, Writing – original draft, Writing – review & editing. **Jianquan Zhong:** Data curation. **Ling Tang:** Investigation, Validation. **Cheekong Chui:** Validation. **Jing Zhang:** Supervision, Project administration, Resources.

Declaration of Competing Interest

The authors declare that they have no known competing financial interests or personal relationships that could have appeared to influence the work reported in this paper.

Data availability

The data that has been used is confidential.

References

- [1] H. Sung, J. Ferlay, R.L. Siegel, et al., Global cancer statistics 2020: GLOBOCAN estimates of incidence and mortality worldwide for 36 cancers in 185 countries, CA Cancer J. Clin. 71 (3) (2021) 209–249.
- [2] C. Şahin, O. Yılmaz, B.A. Üçpinar, et al., Computed tomography-guided transthoracic core needle biopsy of lung masses: technique, complications and diagnostic yield rate, Şişli Etfal Hastanesi tip bülteni 54 (1) (2020) 47–51.
- [3] Y. Wang, W. Li, X. He, et al., Computed tomography-guided core needle biopsy of lung lesions: Diagnostic yield and correlation between factors and complications, Oncol. Lett. 7 (1) (2014) 288–294.
- [4] J.A. Barta, C.A. Powell, J.P. Wisnivesky, Global epidemiology of lung cancer, Ann. Global Health 85 (1) (2019).
- [5] D. Lang, V. Reinelt, A. Horner, et al., Complications of CT-guided transthoracic lung biopsy, Wien. Klin. Wochenschr. 130 (7) (2018) 288–292.
- [6] F. Kong, C. Wang, Y. Li, et al., Advances in study of the sequence of lung tumor biopsy and thermal ablation, Thoracic Cancer 12 (3) (2021) 279–286.
- [7] C. de Margerie-Mellon, C. de Bazelaire, E. de Kerflier, Image-guided biopsy in primary lung cancer: Why, when and how, Diagn. Interventional Imaging 97 (10) (2016) 965–972.
- [8] C. Deng, F. Dai, K. Qian, et al., Clinical updates of approaches for biopsy of pulmonary lesions based on systematic review, BMC Pulmonary Med. 18 (1) (2018) 146.
- [9] K. Nakamura, K. Matsumoto, C. Inoue, et al., Computed tomography-guided lung biopsy: a review of techniques for reducing the incidence of complications, Interventional Radiology 6 (3) (2021) 83–92.
- [10] Y. Zhou, K. Thiruvalluvan, L. Krzeminski, et al., CT-guided robotic needle biopsy of lung nodules with respiratory motion - experimental system and preliminary test, Int. J. Med. Robotics + computer Assisted Surg. 9 (3) (2013) 317–330.
- [11] T. Boskovic, J. Stanic, S. Pena-Karan, et al., Pneumothorax after transthoracic needle biopsy of lung lesions under CT guidance, J. Thoracic Dis. 6 (1) (2014) S99–S107.

- [12] C.J. Walsh, N. Hanumara, A. Slocum, et al. Evaluation of a patient-mounted, remote needle guidance and insertion system for CT-guided, percutaneous lung biopsies, 2007, 2007.
- [13] Y.R. Huo, M.V. Chan, A. Habib, et al., Pneumothorax rates in CT-Guided lung biopsies: A comprehensive systematic review and meta-analysis of risk factors, *Br. J. Radiol.* 93 (1108) (2020) 20190866.
- [14] D. Yin, K. Feng, B. Yan, et al., Analysis of risk factors related to complications of puncture biopsy in lung cancer patients under image guidance, *J. Med. Imaging Health Inform.* 11 (1) (2021) 47–52.
- [15] E.A. Ruud, K. Stavem, J.T. Geitung, et al., Predictors of pneumothorax and chest drainage after percutaneous CT-guided lung biopsy: A prospective study, *Eur. Radiol.* 31 (6) (2021) 4243–4252.
- [16] G.R. Kim, J. Hur, S.M. Lee, et al., CT fluoroscopy-guided lung biopsy versus conventional CT-guided lung biopsy: a prospective controlled study to assess radiation doses and diagnostic performance, *Eur. Radiol.* 21 (2) (2011) 232–239.
- [17] T. Liang, Y. Du, C. Guo, et al., Ultra-low-dose CT-guided lung biopsy in clinic: radiation dose, accuracy, image quality, and complication rate, *Acta Radiol.* 62 (2) (2020) 198–205.
- [18] E. Belbachir, E. Golkar, B. Bayle, et al., Automatic planning of needle placement for robot-assisted percutaneous procedures, *Int. J. Comput. Assisted Radiol. Surg.* 13 (9) (2018) 1429–1438.
- [19] R. Chen, T. Jiang, F. Lu, et al., Semiautomatic radiofrequency ablation planning based on constrained clustering process for hepatic tumors, *IEEE Trans. Biomed. Eng.* 65 (3) (2018) 645–657.
- [20] X. Q. J. M. M. L, et al. An Automatic Path Planning Method of Pedicle Screw Placement Based on Preoperative CT Images. *IEEE Transactions on Medical Robotics and Bionics*, 2022:1.
- [21] L. Wei, S. Jiang, Z. Yang, et al., A CT-guided robotic needle puncture method for lung tumours with respiratory motion, *Physica Med.* 73 (2020) 48–56.
- [22] N. Gerber, B. Bell, K. Gavaghan, et al., Surgical planning tool for robotically assisted hearing aid implantation, *Int. J. Comput. Assist. Radiol. Surg.* 9 (1) (2014) 11–20.
- [23] C.A. Linke, J.J. Camp, K.E. Augustine, et al., Estimating pedicle screw fastening strength via a virtual templating platform for spine surgery planning: a retrospective preliminary clinical demonstration, *Comput. Methods Biomed. Eng.: Imaging & Visualization* 3 (4) (2015) 204–212.
- [24] C. Baegert, C. Villard, P. Schreck, et al., Precise determination of regions of interest for hepatic RFA planning, *Stud. Health Technology Informatics* 125 (2007) 31–36.
- [25] C. Baegert, C. Villard, P. Schreck, et al., Trajectory optimization for the planning of percutaneous radiofrequency ablation of hepatic tumors. *Computer aided surgery* 12 (2007) 82–90.
- [26] C. Villard, L. Soler, A. Gangi, et al., Towards realistic radiofrequency ablation of hepatic tumors 3D simulation and planning, 2004, 2004.
- [27] M. Zeverino, M. Marguet, C. Zulliger, et al., Novel inverse planning optimization algorithm for robotic radiosurgery: First clinical implementation and dosimetric evaluation, *Physica Med.* 64 (2019) 230–237.
- [28] N. Bao, Y. Chen, Y. Liu, et al., Multi-objective path planning for lung biopsy surgery, *Multimedia tools and applications* (2022).
- [29] D. Scorzà, S. El Hadji, C. Cortés, et al., Surgical planning assistance in keyhole and percutaneous surgery: A systematic review, *Med. Image Anal.* 67 (2021), 101820.
- [30] C. Essert, C. Haegelen, F. Lalys, et al., Automatic computation of electrode trajectories for Deep Brain Stimulation: a hybrid symbolic and numerical approach, *Int. J. Comput. Assist. Radiol. Surg.* 7 (4) (2012) 517–532.
- [31] R. Zhang, S. Wu, W. Wu, et al., Computer-assisted needle trajectory planning and mathematical modeling for liver tumor thermal ablation: A review, *Math. Biosci. Eng.: MBE* 16 (5) (2019) 4846–4872.
- [32] A. Seitel, M. Engel, C.M. Sommer, et al., Computer-assisted trajectory planning for percutaneous needle insertions, *Med. Phys. (Lancaster)* 38 (6) (2011) 3246–3259.
- [33] C. Schumann, C. Rieder, S. Haase, et al., Interactive multi-criteria planning for radiofrequency ablation, *Int. J. Comput. Assisted Radiol. Surg.* 10 (6) (2015) 879–889.
- [34] C. Schumann, C. Rieder, S. Haase, et al., Interactive access path exploration for planning of needle-Based interventions, 2013, 2013.
- [35] C. Gao, L. Chen, B. Hou, et al. Precise and semi-automatic puncture trajectory planning in craniofacial surgery: A prototype study, 2014, 2014.
- [36] H. R, E. C, Z. Y, et al. Treatment Planning and Image Guidance for Radiofrequency Ablation of Large Tumors, *IEEE J. Biomed. Health Inform.*, 2014,18(3):920-928.
- [37] J. Li, Y. Xu, N. Shen, et al., A practical pretreatment planning method of multiple puncturing for thermal ablation surgery, *Biocybernetics Biomed. Eng.* 40 (4) (2020) 1469–1485.
- [38] C. Baegert, C. Villard, P. Schreck, et al., Multi-criteria trajectory planning for hepatic radiofrequency ablation, Berlin, Heidelberg: Berlin, Heidelberg: Springer, Berlin Heidelberg (2007) 676–684.
- [39] Y. Chen, Research of Precision improvement and path planning based on lung puncture surgical navigation, Northeast University, 2014.
- [40] N. Bao, The key technologies research of trajectory planning and surgery navigation in CT image-guide lung puncture, Northeast University, 2017.
- [41] J. Zhuang, Research on extraction of thoracic anatomy and path planning based on lung puncture surgical navigation, Northeast University, 2017.
- [42] Y. Cui, Z. Geng, Q. Zhu, et al., Review: Multi-objective optimization methods and application in energy saving, *Energy* 125 (2017) 681–704.
- [43] A. Helck, C. Schumann, J. Aumann, et al., Automatic path proposal computation for CT-guided percutaneous liver biopsy, *Int. J. Comput. Assist. Radiol. Surg.* 11 (12) (2016) 2199–2205.
- [44] R. Zelmann, S. Beriault, M.M. Marinho, et al., Improving recorded volume in mesial temporal lobe by optimizing stereotactic intracranial electrode implantation planning, *Int. J. Comput. Assist. Radiol. Surg.* 10 (10) (2015) 1599–1615.
- [45] N. Hamzé, J. Voisin, P. Collet, et al., Pareto Front vs. Weighted Sum for Automatic Trajectory Planning of Deep Brain Stimulation, Cham, 2016, Springer International Publishing, 2016.
- [46] K. Teichert, A hyperboxing Pareto approximation method applied to radiofrequency ablation treatment planning, Fraunhofer Verlag, Stuttgart, 2014.
- [47] S.M. Bakshmand, R. Eagleson, S. de Ribaupierre, Multimodal connectivity based eloquence score computation and visualisation for computer-aided neurosurgical path planning, *Healthcare Technol. Lett.* 4 (5) (2017) 152–156.
- [48] F. Sun, H. Pei, Y. Yang, et al., A method of lung puncture path planning based on multi-level constraint, *J. Biomed. Eng.* 39 (03) (2022) 462–470.
- [49] S.P. Sahu, B. Kamble, R. Doriya, 3D Lung Segmentation Using Thresholding and Active Contour Method, Singapore, 2020, Springer Singapore, 2020.
- [50] B. Kamble, S.P. Sahu, R. Doriya, A Review on Lung and Nodule Segmentation Techniques, Singapore, 2020, Springer Singapore, 2020.
- [51] L.E. Carvalho, A.C. Sobieranski, A. von Wangenheim, 3D Segmentation Algorithms for Computerized Tomographic Imaging: a Systematic Literature Review, *J. Digit. Imaging* 31 (6) (2018) 799–850.
- [52] H. Duan, G. Su, Y. Huang, et al., Segmentation of pulmonary vascular tree by incorporating vessel enhancement filter and variational region-growing, *J. X-Ray Sci. Technol.* 27 (2019) 343–360.
- [53] S. E G, T. J P, G. E C, et al. FissureNet: A Deep Learning Approach For Pulmonary Fissure Detection in CT Images, *IEEE Transactions on Medical Imaging*, 2019,38 (1):156-166.
- [54] S. Lehmann, N. Frank, An Overview of Percutaneous CT-Guided Lung Biopsies, *J. Radiol. Nursing* 37 (1) (2018) 2–8.
- [55] Y. Cao, L. Xue, B. Qi, et al., Composite Configuration Interventional Therapy Robot for the Microwave Ablation of Liver Tumors, *Chin. J. Mech. Eng.* 30 (6) (2017) 1416–1425.
- [56] A.R. Larici, A. Farchione, P. Franchi, et al., Lung nodules: Size still matters, *Eur. Respiratory Rev.* 26 (146) (2017), 170025.
- [57] L. Liang, D. Cool, N. Nakani, et al., Automatic Radiofrequency Ablation Planning for Liver Tumors With Multiple Constraints Based on Set Covering, *IEEE Trans. Med. Imaging* 39 (5) (2020) 1459–1471.
- [58] B. Guiu, T. De Baere, G. Noel, et al., Feasibility, safety and accuracy of a CT-guided robotic assistance for percutaneous needle placement in a swine liver model, *Sci. Rep.* 11 (1) (2021) 5218.
- [59] M. Mills, J. Choi, G. El-Haddad, et al., Retrospective analysis of technical success rate and procedure-related complications of 867 percutaneous CT-guided needle biopsies of lung lesions, *Clin. Radiol.* 72 (12) (2017) 1038–1046.
- [60] P.P. Bourgouin, K.J. Rodriguez, F.J. Fintelmann, Image-Guided Percutaneous Lung Needle Biopsy: How we do it, *Techniques in Vascular and Interventional Radiology* 24 (3) (2021), 100770.
- [61] Y. Lu, L. Cheng, T. Isenberg, et al., Curve Complexity Heuristic KD-trees for Neighborhood-based Exploration of 3D Curves, *Comput. Graphics Forum* 40 (2) (2021) 461–474.
- [62] A. Asilian Bidgoli, S. Rahnamayan, B. Erdem, et al., Machine learning-based framework to cover optimal Pareto-front in many-objective optimization, Complex & intelligent systems (2022).
- [63] J. Cao, Z. Yan, Z. Chen, et al., A Pareto front estimation-based constrained multi-objective evolutionary algorithm, *Applied Intelligence* (2022).
- [64] Z. Wang, G.P. Rangaiah, Application and Analysis of Methods for Selecting an Optimal Solution from the Pareto-Optimal Front obtained by Multiobjective Optimization, *Ind. Eng. Chem. Res.* 56 (2) (2017) 560–574.
- [65] R. Zhang, Ablation needle trajectory planning method and its application system for CT-guided liver tumor ablation, Beijing University of Technology, 2020.
- [66] A. De León-Cuevas, S. Tovar-Arríaga, A. González-Gutiérrez, et al., Risk map generation for keyhole neurosurgery using fuzzy logic for trajectory evaluation, *Neurocomputing* 233 (2017) 81–89.
- [67] C. Xu, Lung cancer detection and resection planning based on computed tomography images, Shanghai Jiao Tong University (2018).
- [68] Y. Jiang, Q. Song, F. Gao, et al., Needle deformation in the process of puncture surgery: experiment and simulation, *Procedia CIRP* 89 (2020) 270–276.